ARTICLE

Identification of novel synaptonemal complex components in *C. elegans*

Matthew E. Hurlock[1], Ivana Čavka[2], Lisa E. Kursel[3], Jocelyn Haversat[1], Matthew Wooten[1], Zehra Nizami[4], Rashi Turniansky[1], Philipp Hoess[2,5], Jonas Ries[2], Joseph G. Gall[4], Ofer Rog[3], Simone Köhler[2], and Yumi Kim[1]

The synaptonemal complex (SC) is a tripartite protein scaffold that forms between homologous chromosomes during meiosis. Although the SC is essential for stable homologue pairing and crossover recombination in diverse eukaryotes, it is unknown how individual components assemble into the highly conserved SC structure. Here we report the biochemical identification of two new SC components, SYP-5 and SYP-6, in *Caenorhabditis elegans*. SYP-5 and SYP-6 are paralogous to each other and play redundant roles in synapsis, providing an explanation for why these genes have evaded previous genetic screens. Superresolution microscopy reveals that they localize between the chromosome axes and span the width of the SC in a head-to-head manner, similar to the orientation of other known transverse filament proteins. Using genetic redundancy and structure–function analyses to truncate C-terminal tails of SYP-5/6, we provide evidence supporting the role of SC in both limiting and promoting crossover formation.

Introduction

Sexually reproducing organisms rely on the correct execution of meiosis, a specialized cell division that produces haploid gametes to transmit genetic information faithfully from parent to progeny. Errors in this process lead to the production of offspring with an abnormal number of chromosomes, or aneuploidy, which is a major cause of miscarriages and congenital conditions such as Down syndrome (Hassold et al., 2007). Separation of homologous chromosomes during meiosis requires that each chromosome pairs with its homologue and forms a physical linkage during meiotic prophase for their biorientation. The physical connections between homologous chromosomes are established as a result of crossover recombination and are visibly shown as chiasmata. Despite the overall conservation of the meiotic program, including the stereotypical changes chromosomes undergo to achieve biorientation, the molecular players carrying out these functions exhibit a surprising degree of divergence among different lineages.

A striking example of this evolutionary pattern is a zipper-like protein structure called the synaptonemal complex (SC) that reinforces homologue pairing in most eukaryotes (Page and Hawley, 2004). First observed by electron microscopy >60 yr ago (Fawcett, 1956; Moses, 1956), the SC is a hallmark of meiotic prophase and acts as a scaffold for meiotic recombination. The SC consists of two parallel axial elements that form between sister chromatids and a central region with transverse filaments that connect the paired chromosomes. The overall appearance of the SC is highly conserved with respect to its basic dimensions and organization (Zickler and Kleckner, 1999), suggesting that its structural features are essential for interhomologue interactions. Interestingly, the proteins comprising the SC have diverged extensively during evolution. Although genetic and cytological studies have identified SC proteins in various organisms, how individual components interact with each other to form the regular, repetitive arrangement of the SC is largely unknown.

Meiotic recombination initiates with programmed DNA double-strand breaks (Szostak et al., 1983). While excess DNA double-strand breaks are generated during meiotic prophase, only few are ultimately selected to become sites of crossovers (Martinez-Perez and Colaiácovo, 2009). These crossovers are nonrandomly distributed far apart from each other, a phenomenon known as crossover interference (Muller, 1916). Since recombination occurs within the context of the SC, it has been proposed that the presence of crossovers could be communicated through the SC to limit crossover formation (Libuda et al., 2013; Sym and Roeder, 1994). The nematode *Caenorhabditis*

[1]Department of Biology, Johns Hopkins University, Baltimore, MD;   [2]The European Molecular Biology Laboratory, Heidelberg, Germany;   [3]School of Biological Sciences, University of Utah, Salt Lake City, UT;   [4]Department of Embryology, Carnegie Institution for Science, Baltimore, MD;   [5]Collaboration for joint PhD degree between European Molecular Biology Laboratory and Faculty of Biosciences, Heidelberg University, Heidelberg, Germany.

Correspondence to Yumi Kim: yumi.kim@jhu.edu.

elegans represents an extreme case of this regulation where exactly one crossover forms per homologue pair (Hammarlund et al., 2005; Hillers and Villeneuve, 2003; Nabeshima et al., 2004; Yokoo et al., 2012). Recent evidence in *C. elegans* suggests that the SC has liquid-crystalline properties, which enable long-range signal transduction to mediate a chromosome-wide crossover control (Rog et al., 2017). Further support for crossover control by the SC comes from evidence that the presence of crossover-designated sites also influences the dynamic state of the SC (Libuda et al., 2013; Machovina et al., 2016; Pattabiraman et al., 2017; Woglar and Villeneuve, 2018). However, the molecular mechanisms by which the SC regulates crossover still remain poorly understood.

The SC in *C. elegans* exhibits a typical tripartite structure (Goldstein and Slaton, 1982), and its assembly is essential for crossover formation (MacQueen et al., 2002). Axial elements in *C. elegans* comprise meiotic cohesins and four paralogous HORMA domain proteins, High Incidence of Males-3 (HIM-3), Him-Three Paralog-1 (HTP-1), HTP-2, and HTP-3 (Couteau et al., 2004; Couteau and Zetka, 2005; Goodyer et al., 2008; Kim et al., 2014; Martinez-Perez and Villeneuve, 2005; Zetka et al., 1999). Once chromosomes have paired, the central region of the SC assembles. In *C. elegans*, this structure is known to consist of four coiled-coil proteins, SYnaPsis in meiosis abnormal-1 (SYP-1), SYP-2, SYP-3, and SYP-4, which are mutually dependent for SC assembly (Colaiacovo et al., 2003; MacQueen et al., 2002; Smolikov et al., 2007, 2009). These SYP proteins were identified more than a decade ago by forward genetic or yeast two-hybrid screens, and it has been widely believed that this represents the entire set of SC components in *C. elegans*.

Here, we report the identification of two novel SC components, SYP-5 and SYP-6, in *C. elegans*. They transverse the width of the SC, and their recruitment to the SC depends on chromosome axes and other SC components. Interestingly, SYP-5 and SYP-6 are paralogous to each other and play redundant roles in synapsis, which may account for why these proteins have not been identified by previous genetic screens. Using genetic redundancy and structure–function analysis of SYP-5 and SYP-6, we further demonstrate the role of the SC in both limiting and promoting crossover formation. Together, our findings establish SYP-5 and SYP-6 as bona fide components of the SC and shed light on its structure and function.

Results

Identification of SYP-5 and SYP-6 as new SC-associated proteins in *C. elegans*

To gain insight into the organization of the SC, we purified SYP-3–containing protein complexes from a worm strain expressing GFP-SYP-3 (*ieSi11*; Rog and Dernburg, 2015) and analyzed the SC-associated proteins by mass spectrometry (Fig. 1 A). As expected, the four previously known SYP proteins were specifically purified with GFP-SYP-3 (Fig. 1 B). Few other proteins were also enriched in the GFP-SYP-3 immunoprecipitates (Table S1). Among these, we focused on two previously uncharacterized proteins, Y54E10A.12 and F57B10.4, which are homologous to each other, sharing 29% overall sequence identity (Fig. 1 C).

These two proteins are highly expressed in the germline (Kim et al., 2001; Owen et al., 2003) and contain predicted coiled-coil domains (Figs. 1 C and S1 A), a characteristic shared by all known SC components in diverse eukaryotes (de Vries et al., 2005; MacQueen et al., 2002; Page and Hawley, 2001; Sym et al., 1993). Further, they both possess low-complexity sequences in their C-termini, which are conserved in homologues across *Caenorhabditis* species. Based on these characteristics, we hypothesized that Y54E10A.12 and F57B10.4 are novel components of the SC.

To determine whether these proteins are indeed SC components, we first inserted small epitopes, 3xFlag and HA, to the N-terminus of Y54E10A.12 and F57B10.4, respectively, using CRISPR-mediated genome editing and examined their localization by immunofluorescence. Y54E10A.12 and F57B10.4 were initially colocalized within SC-like protein aggregates in the nucleoplasm known as polycomplexes (Roth, 1966; Fig. 2, A and B). Both proteins then loaded onto chromosomes as chromosome pairs and were found along the entire length of chromosomes in pachytene, which perfectly mirrors the localization of SYP-2 (Fig. S1, B and C). These data suggest that Y54E10A.12 and F57B10.4 are novel components of the SC; thus, hereafter, we refer to the genes that encode them as *syp-5* (Y54E10A.12) and *syp-6* (F57B10.4), reflecting their physical order on chromosome I (Fig. 1 D). We note that the level of SYP-6 decreased at the end of pachytene and was no longer detected in diplotene (Fig. S1 C). In contrast, SYP-5 was detected on the "short arm" of the SC in diplotene relative to the crossover site, which defines the site of cohesion loss in meiosis I (Kaitna et al., 2002; Rogers et al., 2002), and persisted until the SC fully disassembled in diakinesis (Fig. S1, B and D), similar to the other SYP proteins in *C. elegans* (Colaiacovo et al., 2003; MacQueen et al., 2002; Smolikov et al., 2007, 2009).

Interestingly, the *C. elegans* genome contains another SYP-5/6-related gene, K09H9.1, on chromosome I (Fig. 1 D). The first two exons of K09H9.1 are pseudogenic fragments of *syp-5*, and the last exon appears to be a pseudogenic fragment of *pha-1*, a gene predicted to have fucosyltransferase activity. Consistent with this, we did not detect the expression of K09H9.1 in the germline when it was tagged with a small epitope at its N-terminus (not depicted). Thus, we conclude that K09H9.1 is a pseudogene derived from a recent gene duplication event in *C. elegans* (see Discussion).

SYP-5 and SYP-6 are localized along the SC between chromosome axes

To establish SYP-5 and SYP-6 as components of the SC, we visualized Flag-SYP-5 and HA-SYP-6 relative to the axial element protein HIM-3 using nuclear spreading and stimulated emission depletion (STED) microscopy. HIM-3 formed two parallel stretches in pachytene nuclei, which were found to be separated by 135 ± 21 nm (Fig. 2, C and D). While this is larger than the previous measurement using single-molecule localization microscopy (SMLM; Köhler et al., 2017), our data are within the range measured using a similar spreading technique (Woglar and Villeneuve, 2018). The N-terminal epitopes for SYP-5 and SYP-6 were localized between the parallel HIM-3 stainings, demonstrating that SYP-5 and SYP-6 are indeed components of the SC central region.
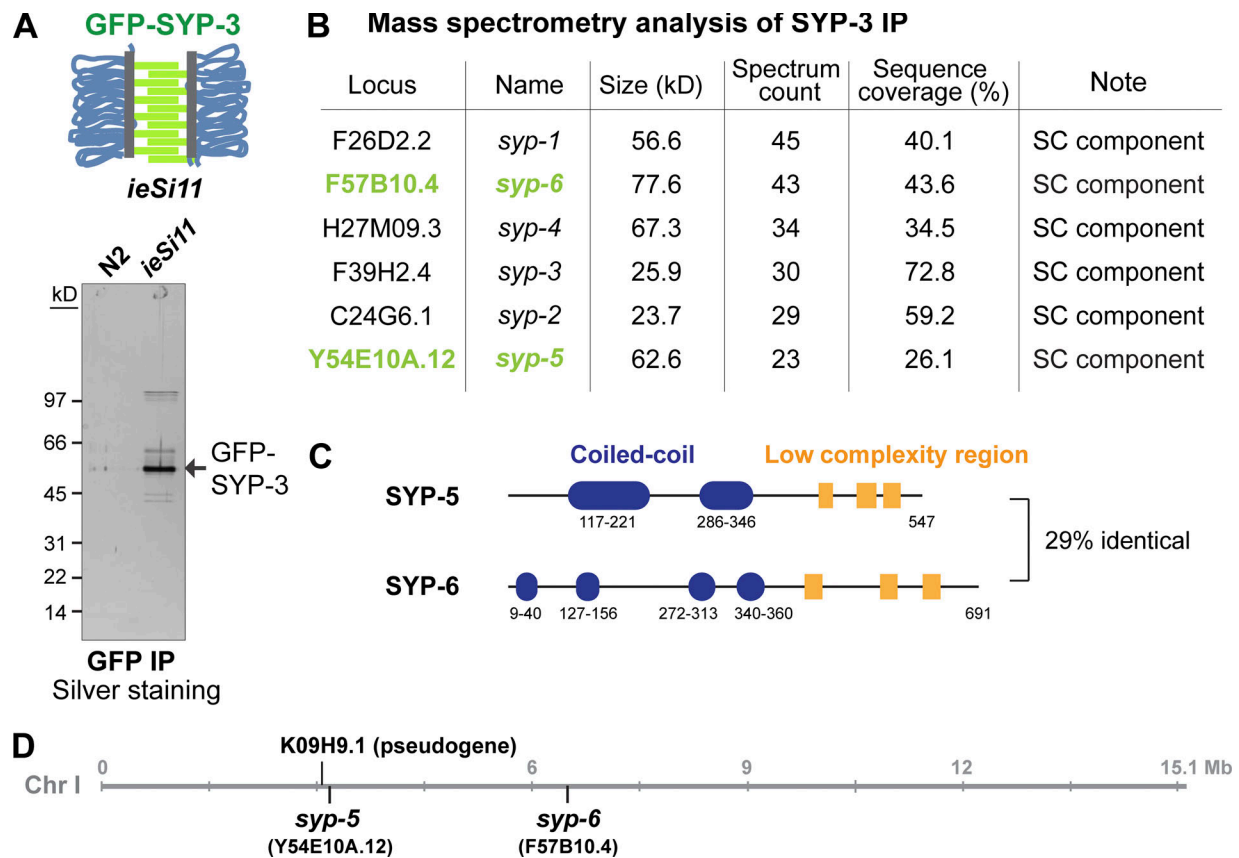
Figure 1. **Identification of SYP-5 and SYP-6. (A)** A schematic of the SC with GFP-SYP-3 is shown on the top (green). Chromosomes are shown in blue and axes in gray. Purified SYP-3–containing protein complexes were separated by SDS-PAGE and visualized by silver staining (bottom). **(B)** List of SYP-3–interacting proteins identified by mass spectrometry. **(C)** A schematic of SYP-5 and SYP-6 showing coiled-coil domains and C-terminal low-complexity sequence domains. **(D)** The genomic location of *syp-5* and *syp-6* and the homologous pseudogene K09H9.1 on chromosome I are shown.

SYP-5 and SYP-6 transverse the width of the SC in a head-to-head manner

Given the extent and the predicted length of the coiled-coil domains of SYP-5 and SYP-6, it is possible that a pair of SYP-5/6 spans the width of the SC, similar to SYP-1 (Schild-Prufert et al., 2011; Woglar and Villeneuve, 2018). Thus, we sought to determine their orientations within the SC using superresolution microscopy techniques. To this end, we used CRISPR to generate worm strains expressing a C-terminal HA tag on either SYP-5 or SYP-6 (Fig. S2 A). By STED microscopy, both SYP-5-HA and SYP-6-HA appeared as a single stretch between the chromosome axes (Fig. S2, B and C), similar to the results obtained using the N-terminal HA-tagged proteins. However, the lateral resolution of STED microscopy (Schermelleh et al., 2019) is close to the width of the SC and may not be sufficient to resolve the two ends of SYP-5 and SYP-6.

We thus employed 3D SMLM and computational analyses to precisely map the positions of the SYP-5 and SYP-6 N- and C-termini relative to HIM-3. Similar approaches have recently been used to determine the organization of chromosome axes in *C. elegans* (Köhler et al., 2017). We estimated the resolution of our SMLM to be 40–60 nm by Fourier ring correlation (Nieuwenhuizen et al., 2013; Fig. S3, A–D), which is sufficient to resolve substructures within the SC. Averaging multiple SC

stretches from SMLM images revealed that the HIM-3 axes were separated by ~128 nm (Fig. 3 C and Fig. S3, F and G), which is consistent with the distance measured by STED. However, a clear distinction emerged between the positions of HA-SYP-5/6 and SYP-5/6-HA. While the N-termini of SYP-5/6 were localized at the center of the SC (Figs. 3 A and S3 G), two distinct stretches of SYP-5-HA and SYP-6-HA were found adjacent to HIM-3, separated by 84 nm in the frontal view (Fig. 3, B and C; and Fig. S3, F and G). Therefore, the C-termini of SYP-5/6 are separated by ~42 nm from their N-termini and are positioned ~21 nm away from the HIM-3 axis. We also note that both ends of SYP-5/6 were confined to a narrow z plane in the cross-sectional view (Fig. 3, A and B, right), with half width at half maximum (HWHM) of 40~50 nm (Fig. S3 F). Together, our results demonstrate that both SYP-5 and SYP-6 span the width of the SC in a head-to-head manner, with the two N-termini positioned at the center and the C-termini facing the axes (Fig. 3 D).

SYP-5 and SYP-6 depend on chromosome axes and other SYP proteins for chromosome loading

To further investigate the behavior of SYP-5 and SYP-6, we raised polyclonal antibodies against the last 14 amino acids of SYP-5 and SYP-6. The affinity-purified antibodies robustly stained the SC in the hermaphrodite germline, which mirrors
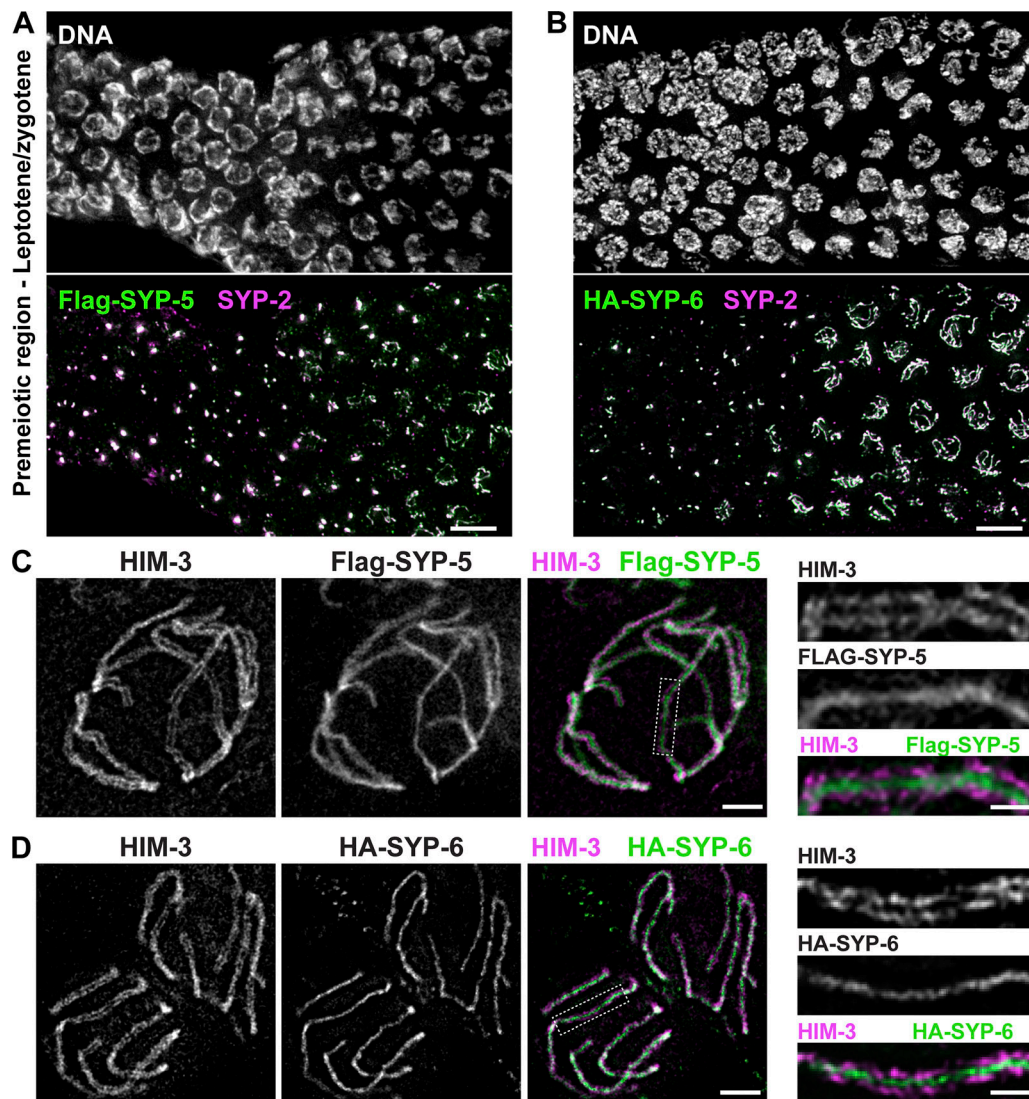
Figure 2. **SYP-5 and SYP-6 are localized between chromosome axes**. **(A and B)** Transition zone nuclei showing DNA (white), Flag-SYP-5 (A) or HA-SYP-6 (B; green), and SYP-2 (magenta). Scale bar, 5 μm. **(C and D)** STED microscopy images showing pachytene nuclei stained for HIM-3 and Flag-SYP-5 (C) or HA-SYP-6 (D). Images represent single z-planes selected to maximize the number of visible SC stretches per nucleus. Scale bar, 1 μm. Insets show zoomed-in view of the SYP-5 or SYP-6 staining between the two chromosome axes (HIM-3) from the boxed regions on the left. Scale bar, 300 nm.

the localization of Flag-SYP-5 and other SYP proteins (Fig. 4 A). To determine the specificity of the antibodies, we generated null alleles for *syp-5* and *syp-6* by targeting their first exons using CRISPR (Fig. S4 A). The antibody raised against the SYP-5 peptide was specific to SYP-5, as the signal on the SC was abolished in *syp-5* mutants, but not in *syp-6* mutants (Fig. S4 B). On the other hand, the antibody raised against the SYP-6 peptide was able to stain the SC in *syp-5* or *syp-6* single mutants, while the signal was completely eliminated in *syp-5 syp-6* double mutants (Fig. S4 C). Thus, the putative SYP-6 antibody recognizes both SYP-5 and SYP-6, and we hereafter refer to it as the SYP-5/6 antibody. Interestingly, the signal for SYP-6, as visualized by the SYP-5/6 antibody in *syp-5* mutants, was diminished at the end of pachytene (Fig. S4 D), confirming our earlier observations with the HA-tagged SYP-6 (Fig. S1 C).

Throughout eukaryotes, SC assembly requires chromosome axes (Colaiacovo et al., 2003; Couteau et al., 2004). As expected,

SYP-5 and SYP-6 failed to load onto chromosomes in mutants lacking an axis component HIM-3 and instead formed poly-complexes together with the other SYPs (Fig. 4 B). Moreover, SYP-5 and SYP-6 were no longer detected in *syp-2* mutants (Fig. 4 B), indicating that SYP-5 and SYP-6 depend on other SC proteins for localization, as is the case for the other SYP proteins (Smolikov et al., 2007, 2009). Taken together, our data demonstrate that SYP-5 and SYP-6 share characteristics found in other SC components.

The evolutionary origin of SYP-5 and SYP-6

In their coding regions, SYP-5 and SYP-6 share 52% sequence identity at the nucleotide level and 29% sequence identity at the protein level. Protein basic local alignment search tool (BLAST) search of *C. elegans* using SYP-5 as a query yields SYP-6 as the top hit, other than SYP-5 itself, suggesting that SYP-5 and SYP-6
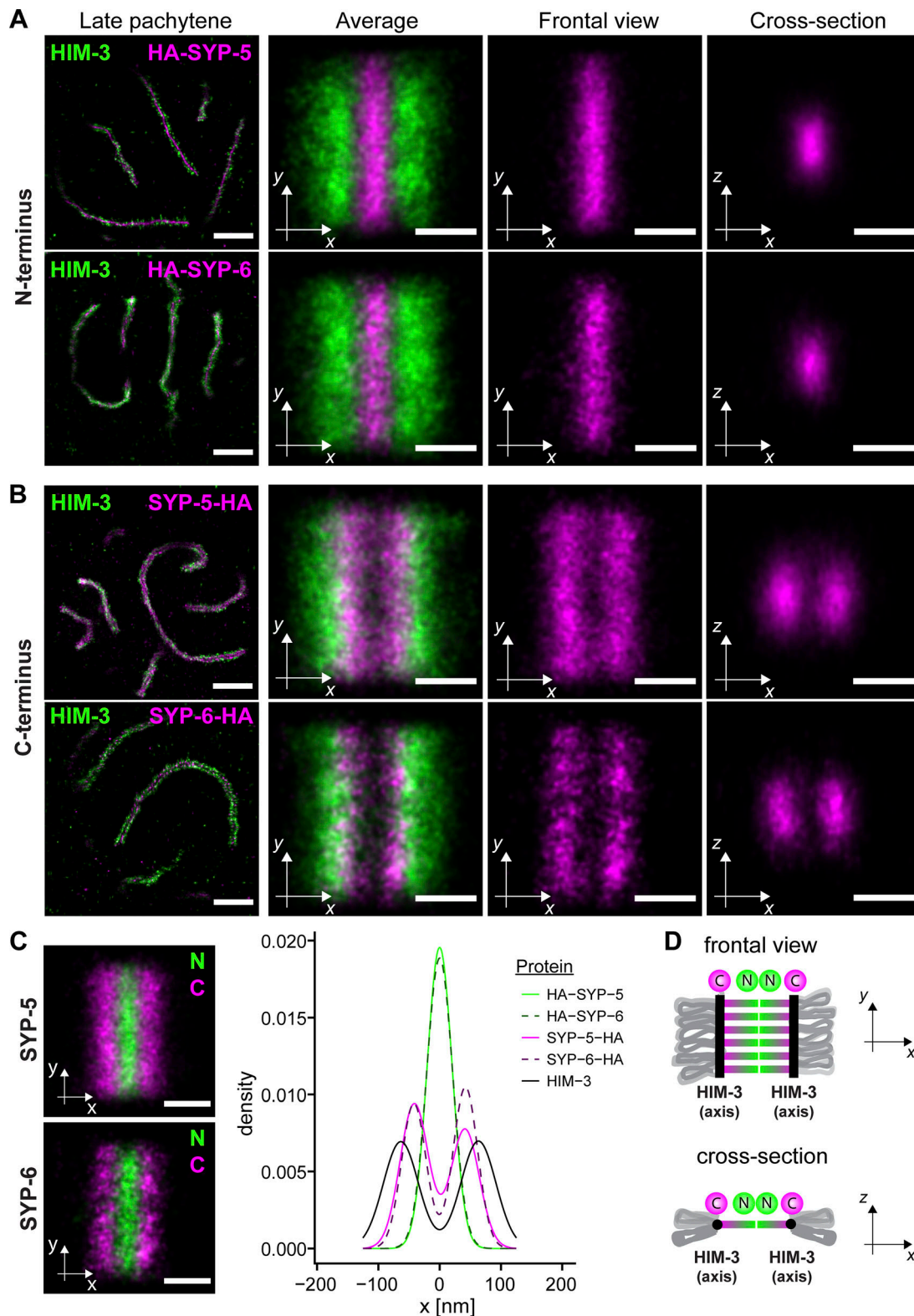
Figure 3. **SYP-5 and SYP-6 transverse the width of the SC in a head-to-head orientation. (A and B)** SMLM images showing late pachytene nuclei (scale bar, 1 µm) stained for HIM-3 and HA fused to N-terminus (A) and C-terminus (B) of SYP-5 and SYP-6 (left). Corresponding images of aligned stretches are shown in frontal (*xy*, center) and cross sectioned (*xz*, right) views. Scale bar, 100 nm. **(C)** Left: Aligned stretches for N-terminus (green) and C-terminus (magenta) of SYP-5 (top) and SYP-6 (bottom). Scale bar, 100 nm. Right: The graph shows the resulting distributions of localizations for all mapped domains in *x*. **(D)** A schematic highlighting the head-to-head orientation of SYP-5/6 within the SC.
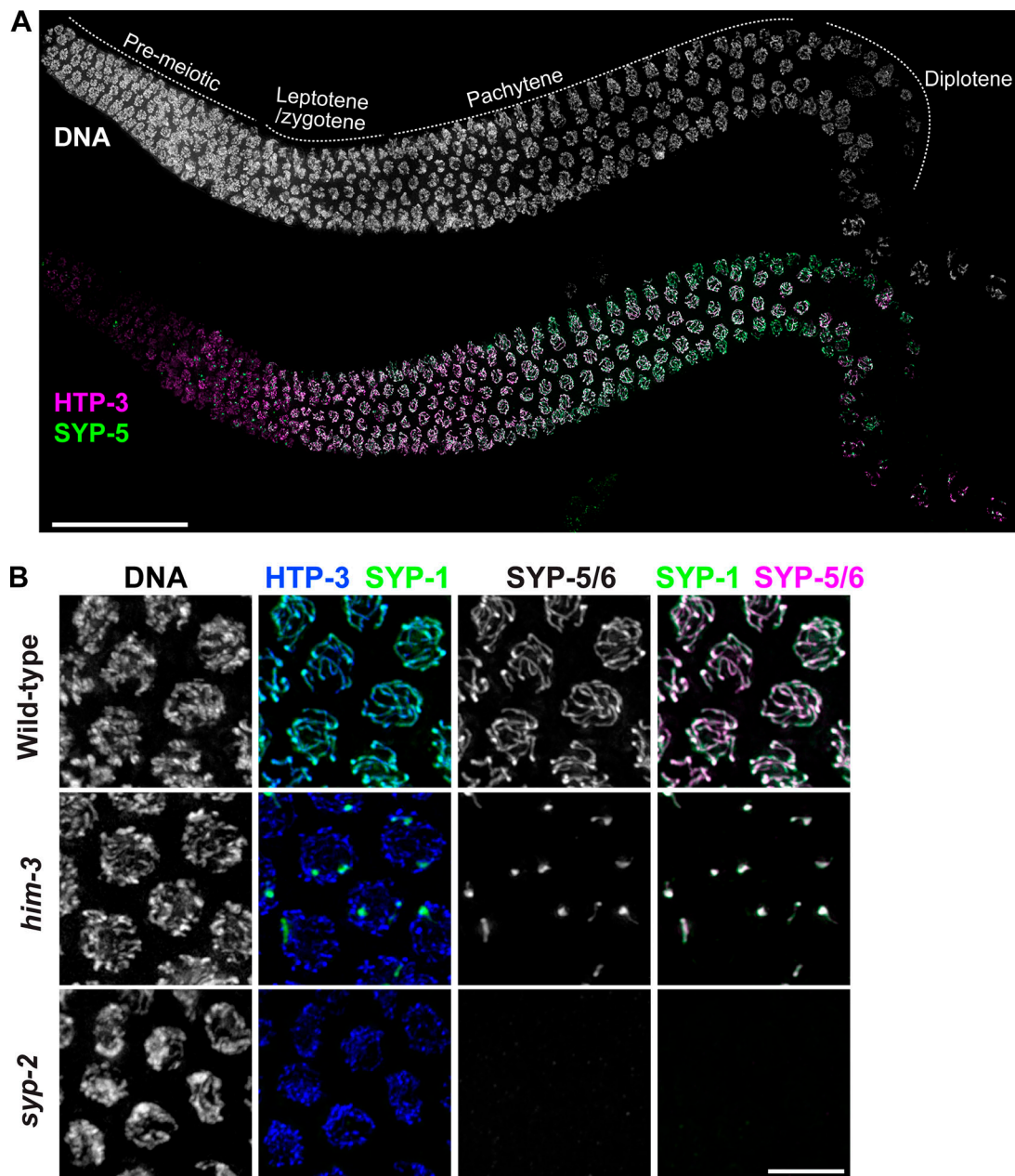
Figure 4. **SYP-5 and SYP-6 depend on chromosome axes and other SYP proteins for chromosome loading. (A)** Composite immunofluorescence images of a whole gonad dissected from a wild-type hermaphrodite showing DNA (white), HTP-3 (magenta), and SYP-5 (green). Scale bar, 50 μm. **(B)** Midpachytene nuclei from wild-type, *him-3*, and *syp-2* mutants were stained for DNA, HTP-3 (blue), SYP-1 (green), and SYP-5/6 (white or magenta). Scale bar, 5 μm.

are paralogs. To determine the evolutionary origins of SYP-5 and SYP-6, we performed translated nucleotide BLAST (tBLASTn) searches of 10 additional *Caenorhabditis* species using *C. elegans* SYP-5 and SYP-6 as queries. All queried species contain a single, high-confidence, BLAST hit. Examination of the syntenic locus of each *syp-5/6*-related orthologue revealed that these genes are present in the same locus as *C. elegans syp-5* (Fig. 5 A). Thus, we refer to each of these *syp-5/6*-related genes as *syp-5.* We also generated a maximum-likelihood phylogeny based on a protein alignment of SYP-5 and SYP-6 sequences from 11 *Caenorhabditis* species. *C. elegans* SYP-5 and SYP-6 were grouped together with high bootstrap support (Fig. 5 B), indicating that they are likely

paralogs born from a recent gene duplication event. Therefore, we conclude that *syp-5* was likely present in the common ancestor of the Elegans and Japonica species groups, making it >30 million years old (Kumar et al., 2017), and that *syp-6* is likely to have arisen from a gene duplication event within the *C. elegans* lineage.

SYP-5 and SYP-6 play partially redundant roles in synapsis
We next examined the effects of deleting *syp-5* and *syp-6*. Self-progeny of hermaphrodites homozygous for the *syp-5* null mutation showed significantly reduced viability (34% vs. 100% in N2), and 15% of surviving progeny were males (compared with
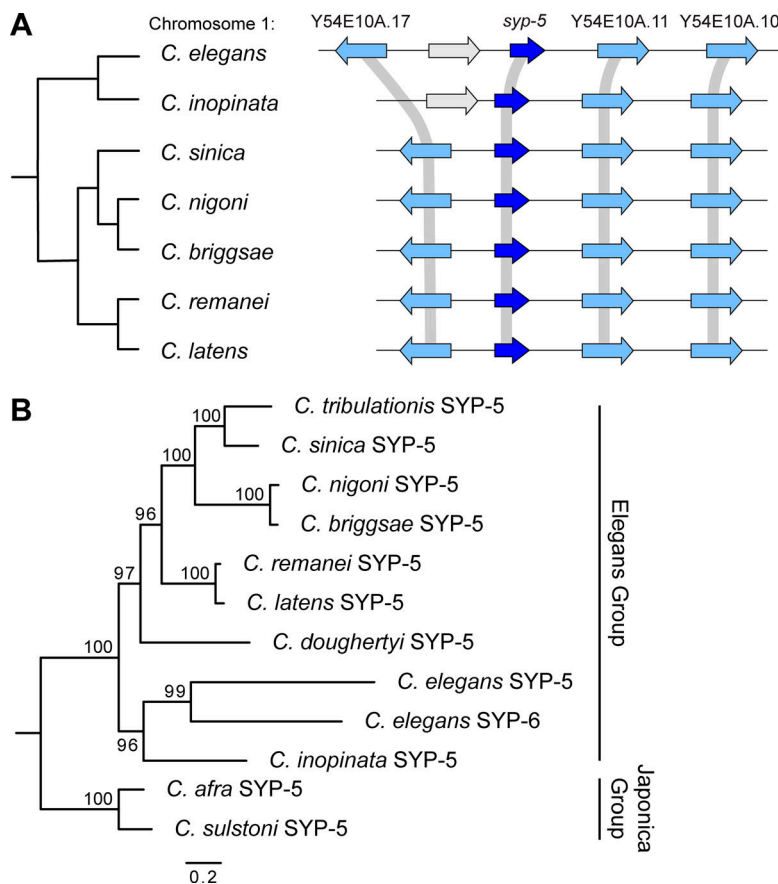
Figure 5. Evolutionary analysis of SYP-5 and SYP-6. (A) A *Caenorhabditis* species cladogram of representative species from the Elegans group. The syntenic locus of *syp-5/6*–related genes is displayed to the right of each species. Genes are represented as colored arrows. Genes that define the genomic context of *syp-5* are displayed in light blue and named according to *C. elegans* gene names. *syp-5* orthologues are displayed in dark blue. Gray lines connect orthologous genes. **(B)** A maximum-likelihood phylogenetic tree made from protein sequences of all *syp-5/6*–related genes identified by tBLASTn. Scale bar represents substitutions per site. Bootstrap values are displayed on each node.

0.1% for wild-type; Fig. S5 A). *syp-6* single mutants, however, did not show obvious phenotypes in meiosis, producing viable progeny (100%; Fig. S5 A). Males in *C. elegans* arise from X-chromosome nondisjunction during meiosis (Hodgkin et al., 1979), and the high incidence of males (Him phenotype) is indicative of errors in meiotic chromosome segregation. In contrast to the single mutants, *syp-5 syp-6* double mutants exhibited a striking drop in viability of progeny to 3%, with an increase in the Him phenotype to 45% among surviving progeny (Fig. S5 A), which is comparable to the phenotypes reported in *syp-1*–null mutants (MacQueen et al., 2002). These results indicate that, while SYP-6 itself is dispensable, both SYP-5 and SYP-6 contribute to proper chromosome segregation during meiosis.

Indeed, SYP-5 and SYP-6 were found to play partially redundant roles in SC assembly. In *syp-5* mutants, completion of synapsis was delayed, and levels of SYP-2 on chromosomes were reduced compared with wild type (Fig. 6 A). Recent evidence has established that defects in synapsis or crossover formation delay meiotic progression by prolonging the kinase activity of Checkpoint kinase 2 (CHK-2; Kim et al., 2015; Rosu et al., 2013; Stamper et al., 2013), which governs homologue pairing, synapsis, and meiotic recombination in *C. elegans* (MacQueen and Villeneuve, 2001). In response to the synapsis defects, the activity of CHK-2 was extended in *syp-5* mutants, as measured by the percentage of germline-length positive for phosphorylation of CHK-2 substrates, HIM-8 and its paralogs (Zinc finger InMeiosis-1 [ZIM-1], -2, and -3), relative to the length from meiotic onset to the end of pachytene (79% in *syp-5* vs. 54% in

wild type; Fig. S5, B and C). Consistent with the egg count Fig. S5 A), animals lacking SYP-6 showed no obvious defects in SC assembly and displayed normal meiotic progression (53% "CHK-2 active zone" in *syp-6*). However, synapsis failed completely in mutants that lacked both SYP-5 and SYP-6 (Fig. 6 A), which further extended CHK-2 activity (84% in *syp-5 syp-6* vs. 54% in wild type; Fig. S5, B and C).

Genetic redundancy between SYP-5 and SYP-6 reveals the role of SC in both limiting and promoting crossover formation

C. elegans has six pairs of chromosomes. Thus, six bivalents are typically found in wild-type oocytes at diakinesis. Oocytes in *syp-5* mutants exhibited an average of seven DAPI-staining bodies (Fig. 6, B and C), indicative of a failure to form crossover in one homologue pair. In *syp-6* mutants, crossovers formed normally for all chromosomes, and six DAPI-staining bodies were visible. However, the number of achiasmate chromosomes dramatically increased to 12 in *syp-5 syp-6* double mutants (Fig. 6, B and C), revealing a complete failure to form crossovers. Quantitative Western blot analysis of an HA tag fused to both SYP-5 and SYP-6 showed that SYP-6 is expressed at only 25–30% of the level of SYP-5, which may provide an explanation for the greater functional contribution by SYP-5 (Fig. 6 D).

The SC mediates robust crossover interference in *C. elegans*, yielding precisely one crossover event per chromosome (Libuda et al., 2013). Thus, we asked whether the redundancy between SYP-5 and SYP-6 could provide a unique opportunity to study the role of the SC in crossover control. Using the protein
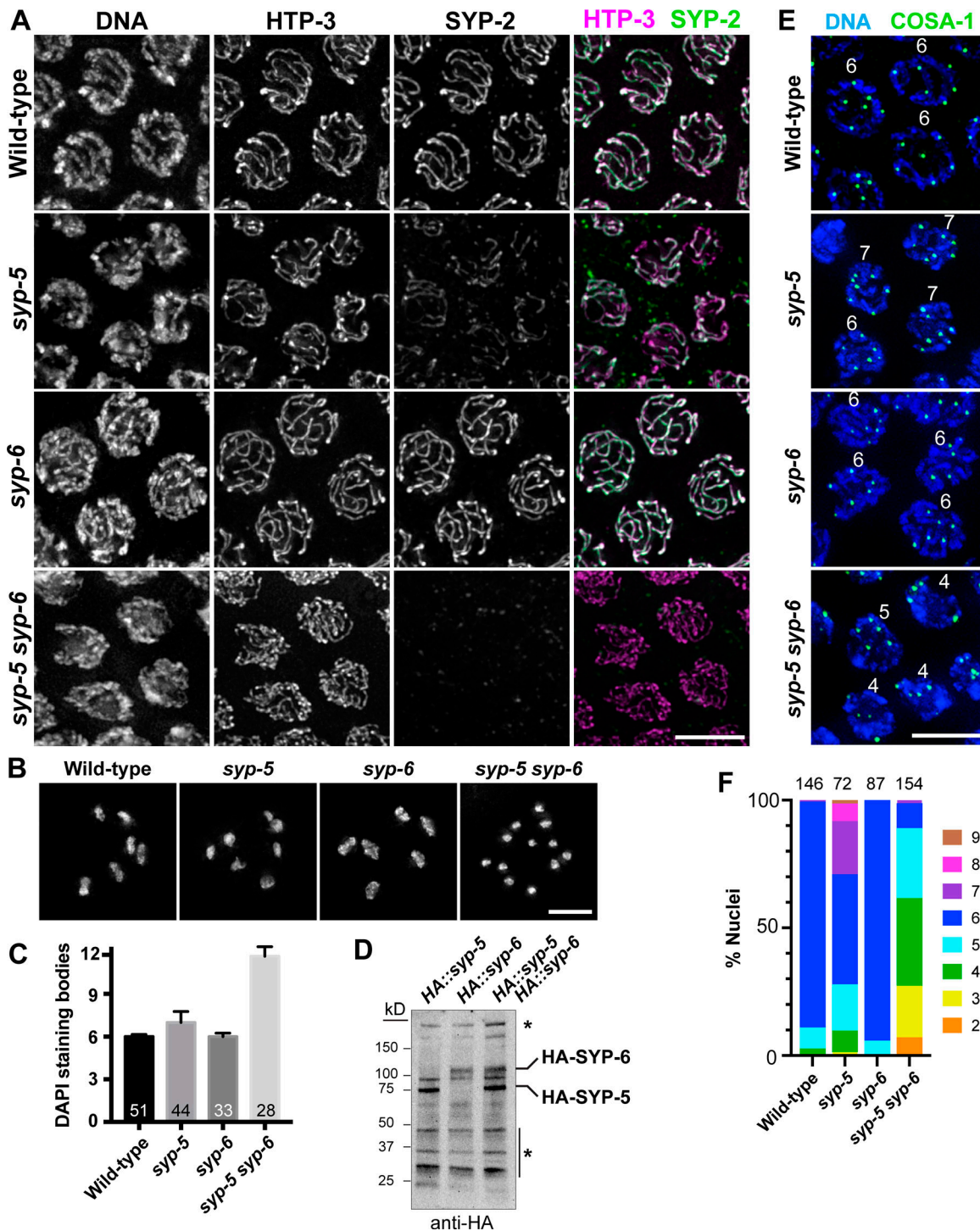
Figure 6. **SYP-5 and SYP-6 play redundant roles in synapsis and crossover formation. (A)** Midpachytene nuclei from wild-type, *syp-5*, *syp-6*, and *syp-5 syp-6* mutants were stained for DAPI, HTP-3, and SYP-2. **(B)** Oocyte nuclei at diakinesis from indicated genotypes were stained with DAPI. **(C)** Graph showing the number of DAPI-staining bodies in oocytes at diakinesis. Error bars indicate SD. Numbers of oocytes scored are indicated below. **(D)** Western blot of worm lysates from indicated strains probed against the HA tag. **(E)** Immunofluorescence of late pachytene nuclei showing DNA (blue) and COSA-1 (green). **(F)** Quantification of COSA-1 foci per nucleus. Numbers of nuclei scored are indicated on the top. All scale bars, 5 µm.

CrossOver Site-Associated-1 (COSA-1) as a cytological marker (Yokoo et al., 2012), we examined how crossovers are designated in the absence of SYP-5 and/or SYP-6. Compared with the invariant 6 COSA-1 foci in the wild-type nucleus, *syp-5* mutants exhibited a wider distribution of four to eight COSA-1 foci (Fig. 6, E and F), supporting a role of the SC in tightly regulating the number of crossovers to one per homologue pair (Hayashi et al., 2010; Libuda et al., 2013). As expected, deletion of *syp-6* did not affect the number of COSA-1 foci, while the *syp-5 syp-6* double mutants displayed two to six COSA-1 foci despite the

absence of chiasmata, consistent with recent evidence shown for other mutants completely lacking the SC (Cahoon et al., 2019; Woglar and Villeneuve, 2018). Therefore, recombination intermediates in the *syp-5 syp-6* double mutants are capable of recruiting crossover-promoting enzymes such as COSA-1; however, those sites cannot mature into crossovers without the SC, and no chiasmata are observed. Taken together, our data support the role of the SC in both limiting and promoting crossover formation.

The acidic C-terminal tails of SYP-5 and SYP-6 are crucial for SC assembly and crossover control

SYP-5 and SYP-6 contain negatively charged regions in their disordered C-termini, which are highly conserved across *Caenorhabditis* species (Fig. 7 A). To determine the significance of these regions in SC assembly, we generated three truncation alleles of *syp-5* and *syp-6* that sequentially remove acidic patches from their C-termini by inserting premature stop codons (Fig. 7 A). Truncated SYP-5 proteins were expressed at similar levels to the full-length protein, except in the strain with the largest deletions of SYP-5 and SYP-6 (SYP-5$^{\Delta 50\ aa}$ SYP-6$^{\Delta 53\ aa}$). SYP-5$^{\Delta 50\ aa}$ was not detectable by Western blot but nevertheless was visible in the germline by immunofluorescence (Figs. S5 E and 7 C). Truncations led to commensurate reduction in egg viability from 99% in wild type to 7% in *syp-5$^{\Delta 50\ aa}$ syp-6$^{\Delta 53\ aa}$*, and the percentage of males among surviving progeny also increased from 2.1% in wild type to 30% in *syp-5$^{\Delta 50\ aa}$ syp-6$^{\Delta 53\ aa}$* (Figs. 7 B and S5 D).

The degree of truncations correlated with the severity of synapsis and crossover defects. SC assembly was greatly delayed, even in *syp-5$^{\Delta 2\ aa}$ syp-6$^{\Delta 2\ aa}$* mutants missing just the last two aspartic acid residues from SYP-5 and SYP-6, and extending the deletions further exacerbated synapsis defects (Figs. 7 C and S5 F). In particular, *syp-5$^{\Delta 50\ aa}$ syp-6$^{\Delta 53\ aa}$* mutants exhibited severe phenotypes such that only one or two SC stretches were found in the nucleus, demonstrating that the C-terminal tails in SYP-5/6 are critical for SC assembly. The number of crossover-designated sites was greatly reduced in all three truncation mutants, and COSA-1 foci were found specifically on synapsed chromosomes (Fig. 7, D and E), reflecting the role of SC in promoting crossover recombination. Surprisingly, more than one COSA-1 focus was frequently detected on a given SC stretch in *syp-5$^{\Delta 50\ aa}$ syp-6$^{\Delta 53\ aa}$* mutants (Fig. 7, D and F), suggesting that crossover control is compromised when the C-terminal acidic patches are removed entirely from SYP-5/6.

To further investigate the contribution of the C-terminal tails of SYP-5/6 on crossover control, we examined the number and distribution of COSA-1 foci along the two-chromosome fusion *mnT12 (IV;X)* in the *syp-5$^{\Delta 50\ aa}$ syp-6$^{\Delta 53\ aa}$* background (Fig. 8 A). The increased length of the *mnT12* chromosome frequently permits the formation of double crossovers, which enables the analysis of crossover interference (Hillers and Villeneuve, 2003; Libuda et al., 2013). While one or two COSA-1 foci were observed on *mnT12* in wild type as previously reported (Libuda et al., 2013; Yokoo et al., 2012), *syp-5$^{\Delta 50\ aa}$ syp-6$^{\Delta 53\ aa}$* mutants displayed 2–5 COSA-1 foci along synapsed *mnT12* (Fig. 8, B and C). 3D tracing revealed that the average distance between COSA-1 foci

on *mnT12* was greatly reduced in *syp-5$^{\Delta 50\ aa}$ syp-6$^{\Delta 53\ aa}$* animals (3.6 µm), compared with the wild type (7.9 µm). Even in instances where *mnT12* had two COSA-1 foci in *syp-5$^{\Delta 50\ aa}$ syp-6$^{\Delta 53\ aa}$* mutants, the average distance between them was significantly smaller (4.6 µm) than that in controls (Fig. 8 D). To determine the effect of deleting SYP-5/6 C-termini on crossover interference, we divided the *mnT12* chromosome into 10 segments (A–J, from the X-chromosome pairing center protein, HIM-8 (Phillips et al., 2005) and binned the position of COSA-1 foci into these segments. In wild-type animals, either a single COSA-1 focus was detected in the middle of *mnT12*, or two COSA-1 foci were observed far apart from each other at opposite ends of the chromosome (Fig. 8 E), consistent with strong crossover interference (Libuda et al., 2013). By contrast, COSA-1 foci were randomly distributed along *mnT12* in *syp-5$^{\Delta 50\ aa}$ syp-6$^{\Delta 53\ aa}$* mutants (Fig. 8 F), indicating that interference is impaired in the absence of SYP-5/6 C-terminal tails.

We also determined whether the additional COSA-1 foci on *mnT12* in *syp-5$^{\Delta 50\ aa}$ syp-6$^{\Delta 53\ aa}$* mutants are resolved into multiple chiasmata, based on the morphology of HTP-3 and the number of SYP-enriched domains in diakinesis nuclei (Martinez-Perez et al., 2008). In wild-type nuclei, either cruciform structures (one chiasma) or ring-like structures (two chiasmata) were observed in *mnT12* (Fig. 8 G). By contrast, the majority of *mnT12* in *syp-5$^{\Delta 50\ aa}$ syp-6$^{\Delta 53\ aa}$* mutants displayed ring-like structures with two chiasmata (58%) or distorted structures with three or more chiasmata (37%; Fig. 8, G and H). Thus, the excess COSA-1 foci observed in pachytene nuclei in the *syp-5$^{\Delta 50\ aa}$ syp-6$^{\Delta 53\ aa}$* background indeed correspond to increased numbers of chiasmata.

Discussion

Here we identify two paralogous proteins, SYP-5 and SYP-6, as components of the SC central region in *C. elegans*. Remarkably, these two genes have evaded identification by genetic screens for more than a decade (Colaiacovo et al., 2002; Srayko et al., 2000), perhaps because loss-of-function mutations of *syp-5* or *syp-6* alone do not cause strong phenotypes. Our biochemical approach has overcome these challenges and enabled the discovery of these two proteins, which function redundantly to promote synapsis.

Our phylogenetic analysis shows that *syp-5* has been duplicated in *C. elegans* to yield *syp-6* and a pseudogene, K09H9.1. Duplication of SYP-5 is expected to be unfavorable, as this would lead to stoichiometric imbalances among the SC components. Indeed, the majority of duplicated genes experience strong purifying selection, especially when the gene product is involved in macromolecular complexes (Lynch and Conery, 2000; Papp et al., 2003). The pseudogene K09H9.1 is likely to have resulted from silencing of a recent *syp-5* duplicate and has acquired degenerative mutations to become nonfunctional. We speculate that several adaptations have helped preserve *syp-6* in *C. elegans* and minimize the dosage imbalance caused by gene duplication. First, SYP-5 and SYP-6 have distinct expression levels. By Western blotting the identical epitope fused to SYP-5 and SYP-6, we have shown that the level of SYP-6 is greatly reduced
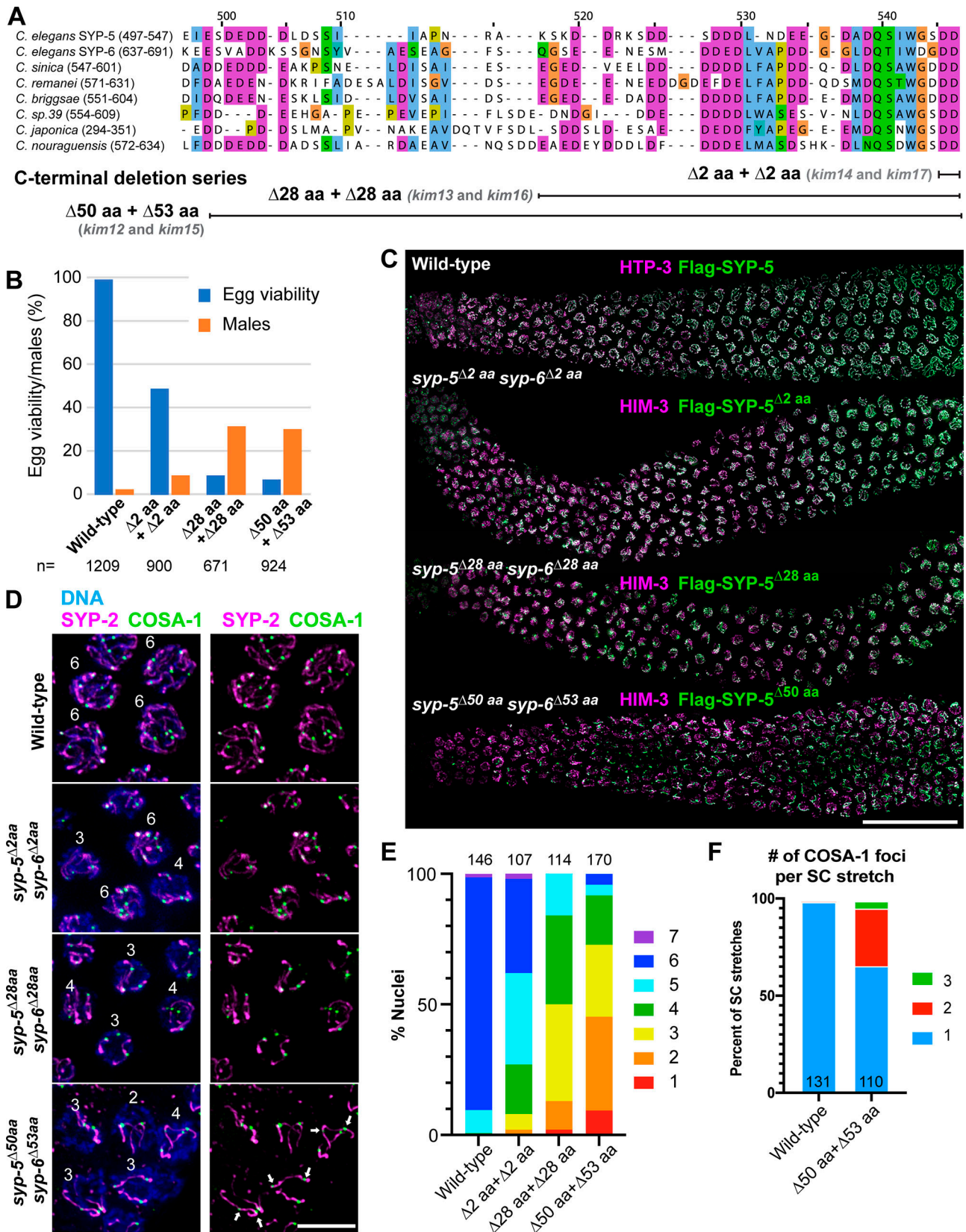
Figure 7. **The C-terminal acidic tails of SYP-5 and SYP-6 are essential for robust synapsis. (A)** Sequence alignment of SYP-5/6 homologues across *Caenorhabditis* species by the T-Coffee algorithm. Schematic of SYP-5 and SYP-6 C-terminal deletions are shown below. Allele designations for *syp-5* and *syp-6* truncations are indicated in parentheses. **(B)** Graph showing percentage egg viability and males from the strains carrying truncation alleles of *syp-5* and *syp-6*. Number of embryos scored for each strain is indicated below the x-axis. **(C)** Composite immunofluorescence images of wild-type and C-terminal truncation

alleles of *syp-5* and *syp-6* showing HTP-3 or HIM-3 (magenta) and Flag-SYP-5 (green) staining. Scale bar, 50 μm. **(D)** Immunofluorescence images of late pachytene nuclei stained for DNA (blue), SYP-2 (magenta), and GFP-COSA-1 (green). Arrows in the lower right panel indicate incidences of multiple COSA-1 foci per SC stretch. Scale bar, 5 μm. **(E)** Graph showing the quantification of the number of COSA-1 foci found in late pachytene nuclei from the indicated strains. Numbers of nuclei scored are shown on the top. **(F)** Graph showing the number of COSA-1 foci per SC stretch in wild-type and *syp-5*$^{\Delta 50\ aa}$ *syp-6*$^{\Delta 53\ aa}$ mutants. Numbers of nuclei scored are shown below.

compared with SYP-5 (Fig. 6 D). In addition, the expression of SYP-6 decreases abruptly in late pachytene, while SYP-5 persists on the SC short arm until its complete disassembly in diakinesis (Figs. S1 and S4). The mechanism underlying the distinct regulation of SYP-6 is unclear. Although SYP-6 itself is dispensable for meiosis, it nevertheless contributes to synapsis and crossover formation in the absence of SYP-5. Thus, duplication of *syp-5* may buffer against the effect of harmful mutations and provide a selective advantage to retain both copies, providing an example of subfunctionalization of duplicated genes (Force et al., 1999; Lynch and Force, 2000).

Using superresolution microscopy, we demonstrate that SYP-5 and SYP-6 span the width of the SC with their N-termini localized at the center and the C-termini facing the chromosome axes (Fig. 3). This suggests that the *C. elegans* SC is unique in containing multiple transverse filament proteins: SYP-1 and SYP-5/6 (Schild-Prufert et al., 2011; Woglar and Villeneuve, 2018). SYP-1 and SYP-5/6 show no homology other than short stretches (<10 amino acids) within their coiled-coil domains. Interestingly, the extent of coiled-coils and the overall size of SYP-1 and SYP-5/6 are significantly smaller than in other transverse filament proteins (e.g., yeast Zip1, *Drosophila* C(3)G, Arabidopsis ZYP1, and mammalian SYCP1), despite the conserved appearance of the *C. elegans* SC on electron micrographs (Colaiacovo et al., 2003; Rog et al., 2017). Thus it is unclear whether SYP-1 and SYP-5/6 interact with each other to form a homo- or heterotetramer through their N-terminal domains, as shown for SYCP1 (Dunce et al., 2018; Liu et al., 1996), or form tetramers through their coiled-coils, as suggested for Zip1 (Dong and Roeder, 2000). Alternatively, the N-termini of SYP-1 and SYP-5/6 could be connected indirectly by other SYP proteins comprising the central element. Nevertheless, the head-to-head orientation has been observed for all known transverse filament proteins from diverse eukaryotes (Anderson et al., 2005; Cahoon et al., 2017; Dong and Roeder, 2000; Schücker et al., 2015), suggesting that this architecture of the SC is widely conserved.

Our work reveals conserved motifs within SYP-5/6 that are crucial for SC assembly. Truncating the C-terminal acidic sequences of SYP-5/6 causes severe synapsis defects, and extending the deletion results in progressively fewer SC stretches (Fig. 7), suggesting that the overall charge of SYP-5/6 C-termini might be critical for proper synapsis. Previous evidence from yeast and *Drosophila* has shown that the C-terminal domain of transverse filament proteins is essential for tethering the SC to chromosome axes (Jeffress et al., 2007; Tung and Roeder, 1998). However, robust SC stretches do form in our C-terminal truncation mutants of SYP-5/6, which could be attributed to the presence of the additional transverse filament SYP-1 in *C. elegans*. Interestingly, our SMLM data show that the C-termini of

SYP-5/6 are separated by ∼21 nm from the most proximal axis component, HIM-3 (Köhler et al., 2017), suggesting that SYP-5/6 do not tightly associate with the chromosome axis. Consistent with this, we did not find any axis components in our SYP-3 immunoprecipitates and vice versa from our previous purification of the chromosome axis (Kim et al., 2014). Thus, how the SC interfaces the chromosome axis and preferentially assembles between the axes remains unknown. Moreover, whether and how the C-terminal tails of SYP-5/6 are involved in protein–protein interactions with other SYP proteins will be important questions for the future.

Using genetic redundancy and structure–function analyses to truncate C-terminal tails of SYP-5/6, we have provided evidence supporting the role of SC in crossover regulation. Increased incidence of crossover designation in *syp-5* mutants is very much in line with the phenotypes observed when SYP-1 levels are reduced by partial RNAi (Hayashi et al., 2010) and supports the role of SC in limiting crossovers to one per homologue pair (Libuda et al., 2013). In *syp-5 syp-6* double mutants, crossover-promoting enzymes are found to be recruited to multiple nuclear foci, despite the fact that no crossovers form in these mutants (Fig. 6). This is in agreement with recent evidence that the SC directs crossover-promoting activities and facilitates interhomologue recombination (Cahoon et al., 2019; Rog et al., 2017), potentially by confining crossover-designated sites in a bubble-like structure (Woglar and Villeneuve, 2018). Synapsis defects caused by the C-terminal truncations of SYP-5/6 correlate with a reduced number of crossover designations, and crossover factors are always found on synapsed chromosomes (Fig. 7 D), reflecting the role of the SC in promoting crossover formation (Cahoon et al., 2019). However, deletion of the entire acidic C-terminal tail causes stronger defects in SC assembly and increases the incidence of multiple crossover intermediates per SC stretch, indicating that the chromosome-wide signaling to control crossover number is impaired in these mutants.

Recent evidence suggests that the SC has liquid crystalline–like properties, thereby serving as a phase-separated compartment to mediate a chromosome-wide crossover control (Rog et al., 2017). Many examples of phase-separated cellular bodies are characterized by the presence of intrinsically disordered proteins with stretches of low-complexity sequences (Shin and Brangwynne, 2017). Indeed, SYP-5 and SYP-6 contain highly conserved low-complexity sequences in their C-termini, which include the acidic patches that are shown here to play important roles in SC assembly (Fig. 7). It remains to be determined whether these regions within SYP-5/6, as well as disordered regions in other SYP proteins, contribute to the liquid crystalline properties of the SC. Future mapping of protein–protein interactions among the SYP proteins and analysis of structural changes within the SC upon crossover designation will provide crucial insights into their roles in crossover regulation.
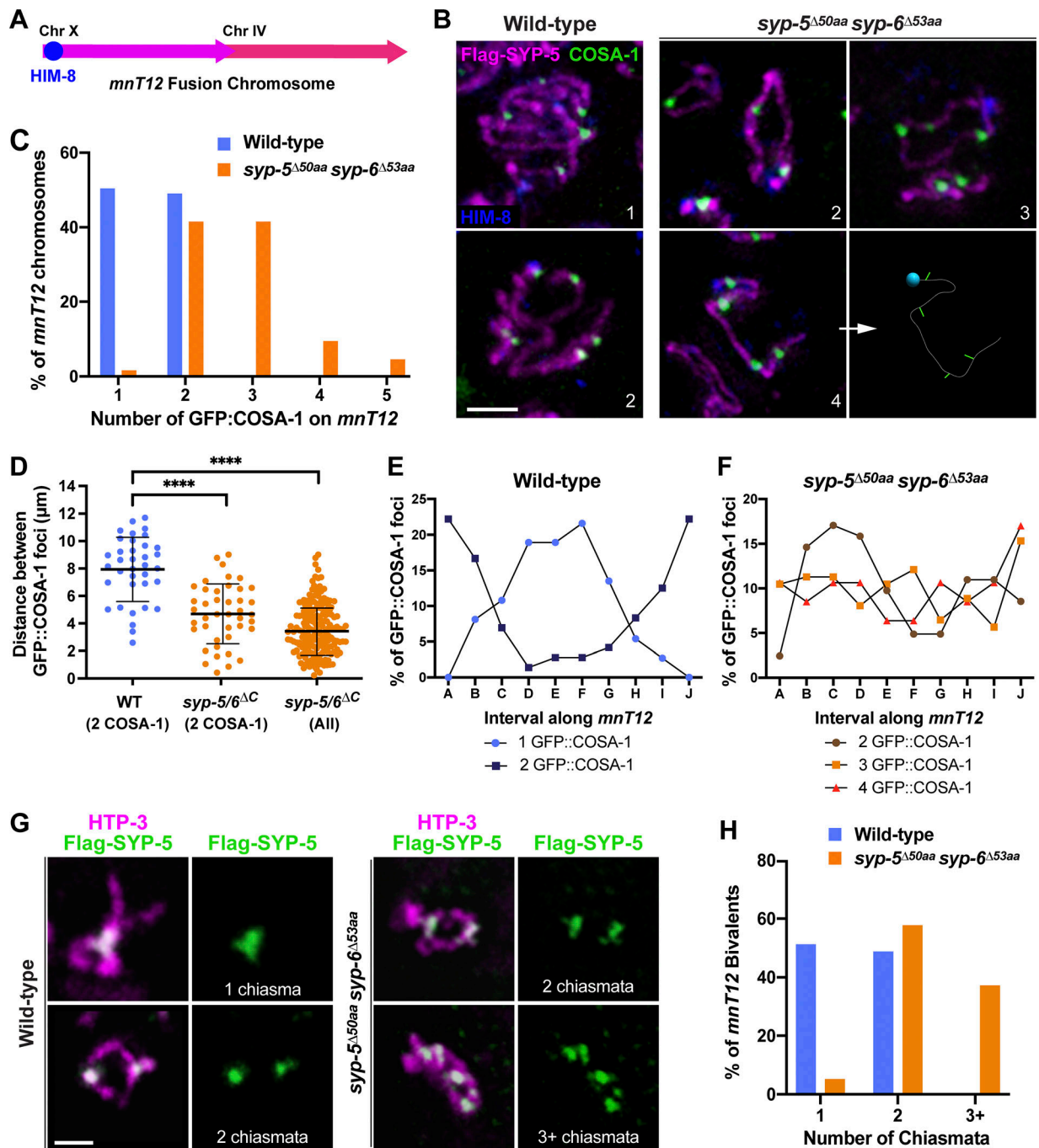
Figure 8. **The C-terminal acidic tails of SYP-5 and SYP-6 are essential for crossover control. (A)** Schematic of the *mnT12* (IV;X) fusion chromosome. HIM-8 (blue) was used to identify the *mnT12* chromosome. **(B)** Immunofluorescence images of late pachytene nuclei in wild-type (left) and *syp-5*$^{\Delta 50 \, aa}$ *syp-6*$^{\Delta 53 \, aa}$ mutants (right) stained for HIM-8 (blue), Flag-SYP-5 (magenta), and GFP-COSA-1 (green). The number of COSA-1 foci on *mnT12* is indicated in the lower right corner of each image. An example of 3D tracing of COSA-1 foci along synapsed *mnT12* is shown at the lower right image. Scale bar, 2 μm. **(C)** Histogram showing the percentage of *mnT12* with the indicated number of COSA-1 foci for the wild-type (*n* = 73) and *syp-5*$^{\Delta 50 \, aa}$ *syp-6*$^{\Delta 53 \, aa}$ mutants (*n* = 104). **(D)** Scatterplot showing the distance between COSA-1 foci on *mnT12* in wild-type (7.9 ± 2.3 μm, *n* = 36) and *syp-5*$^{\Delta 50 \, aa}$ *syp-6*$^{\Delta 53 \, aa}$ mutants (4.6 ± 2.2 μm, *n* = 42) with two COSA-1 foci, and on all *mnT12* in *syp-5*$^{\Delta 50 \, aa}$ *syp-6*$^{\Delta 53 \, aa}$ mutants with multiple foci (3.6 ± 1.8 μm, *n* = 184). Mean distance and SD are indicated in black horizontal lines. The distances between COSA-1 foci in *syp-5*$^{\Delta 50 \, aa}$ *syp-6*$^{\Delta 53 \, aa}$ mutants were significantly smaller than that in wild-type (****, P < 0.0001) by two-tailed, Mann–Whitney *U* test. **(E and F)** Graphs showing the distribution of COSA-1 foci along *mnT12* in wild-type (E) and *syp-5*$^{\Delta 50 \, aa}$ *syp-6*$^{\Delta 53 \, aa}$ mutants (F). The *mnT12* chromosome was divided into 10 equidistant intervals, and the position of COSA-1 was scored. **(G)** Partially projected immunofluorescence images of *mnT12* bivalents in diakinesis stained for HTP-3 (magenta) and Flag-SYP-5 (green). The number of chiasmata on *mnT12* is indicated. Scale bar, 2 μm. **(H)** Histogram showing the percentage of *mnT12* bivalents with the indicated number of chiasmata for the wild-type (*n* = 82) and *syp-5*$^{\Delta 50 \, aa}$ *syp-6*$^{\Delta 53 \, aa}$ mutants (*n* = 77).

Materials and methods

C. elegans strains and egg count

All strains were maintained on nematode growth medium (NGM) plates at 20°C under standard conditions. N2 Bristol was used as the wild-type strain. The mutations and strains used in this study are summarized in Table S2, Table S3, and Table S4. To score egg viability and male progeny, L4 hermaphrodites were picked onto individual plates and counted immediately after each laying period, and surviving progeny were scored when worms reached adult stage.

Immunoprecipitation and mass spectrometry analysis of SYP-3–containing protein complexes

C. elegans strain expressing GFP-SYP-3 (ieSi11; Rog and Dernburg, 2015) was synchronously grown in liquid culture at 20°C until worms reach the young adult stage. Animals were harvested by sucrose flotation, snap frozen in liquid nitrogen, and disrupted using a mixer mill (Retsch). To enrich for nuclear fractions, ground worms were incubated in hypotonic buffer (5 mM Tris-HCl, pH 8.0, 40 mM KCl, 1 mM EDTA, 0.3 mM spermidine, 0.15 mM spermine, and Roche protease inhibitor cocktail). Cells were homogenized in a Dounce homogenizer and spun at 100 g for 3 min to separate nuclei from large debris. The supernatant was spun at 2,000 g for 15 min to pellet the nuclei, and the pellet was resuspended in nuclei buffer (10 mM Tris-HCl, pH 8.0, 80 mM KCl, 2 mM EDTA, 0.75 mM spermidine, 0.3 mM spermine, and Roche protease inhibitor cocktail). The nuclei were further purified by centrifugation over a sucrose cushion (30% wt/vol in nuclei buffer) at 2,000 g for 15 min. The pellet containing nuclei was resuspended in lysis buffer (50 mM Hepes, pH 7.4, 1 mM EGTA, 1 mM MgCl$_2$, 100 mM KCl, and 10% glycerol) containing 5 mM CaCl$_2$ and treated with 200 units/ml of micrococcal nuclease (NEB) for 1 h at room temperature to digest chromatin. Cleared extracts were used for immunoprecipitation of SYP-3–containing protein complexes using a GFP-binding protein coupled to a HiTrap NHS-activated column (GE Healthcare). Bound proteins were eluted with 0.1 M glycine, pH 2.5, and eluted fractions were immediately neutralized by addition of Tris base. Trypsin-digested samples were analyzed for protein identification by MudPIT.

Generation of C. elegans strains by CRISPR-mediated genome editing

To generate strains expressing 3Flag-SYP-5, HA-SYP-5, SYP-5-HA, HA-SYP-6, and SYP-6-HA, N2 worms or worms expressing GFP-COSA-1 were injected with 16 µM Cas9 protein complexed with 16 µM trans-activating CRISPR RNA (tracrRNA)/crRNA oligonucleotides (IDT), pCFJ104 (5 ng/µl), and pCFJ90 (2.5 ng/µl), together with a single-stranded DNA oligonucleotide (100 ng/µl; IDT) as a repair template (see Table S2 and Table S3), using an Olympus IX51 inverted microscope fitted with a Narishige micromanipulator and an Eppendorf Femtojet microinjector. F1 progeny were singled to individual plates to self-propagate and were screened for successful edits via PCR.

For generating null alleles of syp-5 and syp-6, N2 worms were injected with 16 µM Cas9 protein complexed with 16 µM tracrRNA/crRNA oligonucleotides (IDT), together with pCFJ104 (5 ng/µl) and pCFJ90 (2.5 ng/µl), to induce DNA double-strand breaks within the first exons of syp-5 and syp-6, respectively.

Antibody production

Polyclonal HIM-3 antibodies were raised against a full-length recombinant HIM-3 protein (Kim et al., 2014) in chicken (Pocono Rabbit Farm) and were purified from the immune serum using the HIM-3 protein coupled to a HiTrap NHS-activated column (GE Healthcare). For SYP-5 and SYP-6 antibodies, synthetic phospho-peptides corresponding to the C-terminus of SYP-5 (CEEGDADQpSIWGSDD; Biomatik) and SYP-6 (CDDGGLDQpTIWDGDD) were coupled to maleimide-activated keyhole limpet hemocyanin (Thermo Fisher Scientific) and used for immunization of rabbits (Pocono Rabbit Farm). Polyclonal SYP-5 and SYP-5/6 antibodies were affinity purified from the immune sera using HiTrap NHS-activated columns (GE Healthcare) coupled to the same SYP-5 and SYP-6 peptides, respectively.

Chromosome spreading and STED microscopy

Chromosome spreads were prepared from 20–40 adult hermaphrodites dissected in 5 µl dissecting solution (85% vol/vol HBSS [Gibco] and 0.1% vol/vol Tween-20) on an ethanol-washed 22 × 22–mm coverslip. 50 µl of spreading solution (2.5% wt/vol PFA, 2% wt/vol sucrose, 0.32% vol/vol Lipsol, and 0.04% wt/vol sarcosyl) was added, and dissected gonads were immediately dispersed across the coverslip using a pipette tip. Coverslips were dried at room temperature for >5 h, washed in methanol at –20°C for 20 min, and rehydrated with PBS with Tween (PBST). Samples were then processed for immunofluorescence.

STED microscopy was performed using a Leica TCS SP8 microscope equipped with a 100× oil-immersion, 1.4-NA STED white objective and a Lecia HyD detector. Single z-plane images were acquired at room temperature using Leica LAS-X software. Fluorescent secondary antibodies were systematically tested for optimal multicolor STED imaging: Alexa Fluor 488 was depleted with STED 592-nm laser, and Alexa Fluor 594, CF 633, and Alexa Fluor 647 were depleted with STED 775-nm laser. 100 nm TetraSpeck microsphere beads (Thermo Fisher Scientific) were used to validate the STED efficiency and adjust for thermal drift during image acquisition. Slides were mounted using ProLong Diamond (Invitrogen). Image processing was performed using the Scientific Volume Imaging Huygens Professional software package.

Evolutionary analysis of SYP-5 and SYP-6

Caenorhabditis syp-5 and syp-6 orthologues were identified by using C. elegans SYP-5 and SYP-6 to query 10 Caenorhabditis species genomes using tBLASTn (Altschul et al., 1997) implemented in WormBase or Caenorhabditis.org genome databases. All queries produced a single, high-confidence hit to an annotated gene. The syp-5 coding sequence in C. afra required manual editing of one intron-exon boundary that caused the resulting protein sequence to be artificially truncated. The C. afra syp-5 sequence was corrected based on alignment to a closely related species, C. sulstoni, and produced a full-length SYP-5 protein after curation. We annotated the syntenic locus

Hurlock et al.
Identification of new SC components in C. elegans

Journal of Cell Biology   13 of 17
https://doi.org/10.1083/jcb.201910043

of each identified *syp-5/6*-related gene according to orthologous genes in *C. elegans*, and *syp-5/6*-related genes were named according to their shared syntenic location. SYP-5 and SYP-6 protein sequences were aligned using ClustalW (Larkin et al., 2007) implemented in Geneious Prime 2019.0.4. Alignments were further refined manually, including removal of gaps. Maximum likelihood phylogenetic trees of SYP-5 and SYP-6 protein sequences were generated using the LG substitution model in PhyML, implemented in Geneious (Guindon et al., 2010), using 100 bootstrap replicates for statistical support. Phylogenies are rooted on the common ancestor of the Elegans and Japonica species groups.

Immunofluorescence and quantification of COSA-1 foci

Germlines were dissected from 24-h post-L4 adults in egg buffer (25 mM Hepes, pH 7.4, 118 mM NaCl, 48 mM KCl, 2 mM EDTA, 5 mM EGTA, 0.1% Tween-20, and 15 mM NaN$_3$) and fixed in 1% formaldehyde before freezing in liquid nitrogen. Dissected germlines were further fixed in methanol at –20°C for 1 min and rehydrated with PBST. Samples were then blocked with blocking reagent (Roche) for 1 h and incubated with primary antibodies overnight at 4°C. Primary antibodies were used at the following concentrations: FLAG (mouse, 1:500; Sigma F1804), HA (rat, 1:500; Chromotek, 7C9), SYP-2 (rabbit, 1:500; Colaiacovo et al., 2003), SYP-1 (goat, 1:500; MacQueen et al., 2005), HTP-3 (guinea pig, 1:500; MacQueen et al., 2005), HIM-3 (chicken, 1:500; this study), GFP Booster (1:200; Chromotek), HTP-1/2 (rabbit, 1:500; Martinez-Perez et al., 2008), phospho-HIM-8/ZIMs (rabbit, 1 µg/ml; Kim et al., 2015), HIM-8 (rat, 1:500; Phillips et al., 2005), SYP-5 (rabbit, 1:500; this study), and SYP-5/6 (rabbit, 1:500; this study). Slides were washed with PBST three times for 10 min each and incubated with secondary antibodies for 1–2 h. Secondary antibodies labeled with Alexa Fluor 488, 555, 594, or 647 or CF633 were purchased from Invitrogen or Sigma and used at 1:200 dilution. Washed slides were mounted using ProLong Gold (Invitrogen). Images were acquired at room temperature using a DeltaVision Elite system (GE) equipped with a 100× oil-immersion, 1.4 NA objective and a scientific complementary metal–oxide–semiconductor camera (PCO). 3D image stacks were collected at 0.2-µm intervals, processed by iterative deconvolution (enhanced ratio, 20 cycles), and projected using the SoftWoRx package. Composite images were assembled and colored using Adobe Photoshop.

For quantification of GFP-COSA-1 foci, COSA-1 foci were counted in nuclei at least three rows after their first appearance in the germline. Only the foci colocalizing with HTP-3 were counted. *mnT12* chromosomes were identified by HIM-8 staining, and continuous SC stretches (visualized by Flag-SYP-5 immunofluorescence) were traced in three dimensions using the Imaris FilamentTracer tool (Bitplane). The positions of COSA-1 foci were recorded along the length of synapsed *mnT12* and normalized by dividing the measured length of each *mnT12* chromosome into 10 evenly spaced intervals and binning the foci positions into these intervals.

For quantification of chiasmata formation, *mnT12* chromosomes were identified in diakinesis nuclei based on their size,

and only the ones that were unambiguously distinct from other DAPI bodies were scored for the number of chiasmata (1, 2, or ≥3) based on morphology of HTP-3 staining and the number of FLAG-SYP-5-enriched domains.

SMLM

Sample preparation

For SMLM, coverslips (Precision coverslips, 24 mm, Carl Roth) were cleaned by a 10-min wash in ethanol, rinsed in milli-Q water, and plasma cleaned (PlasmaPrep2, GaLa Instrumente). Clean slides were incubated with 0.01% poly-L-lysine (30,000–70,000 D, Sigma-Aldrich) for 10 min. After incubation, coverslips were rinsed in milli-Q water and dried at room temperature. Poly-L-lysine–coated coverslips were stored at 4°C until use.

Immunofluorescence samples for SMLM imaging were prepared as described above with a few modifications. Worms were immobilized in 0.02% of tetramisole during dissection and fixed with 1% PFA on poly-L-lysine–coated coverslips. Primary antibodies used for SMLM were: anti-HA (1:200, mouse monoclonal 2-2.2.14, Thermo Fisher Scientific), anti-HIM-3 (1:200 or 1:100, rabbit polyclonal 53470002, Novus Biologicals). Secondary antibodies were Alexa Fluor 647 anti-mouse (1:1,000 or 1:500, donkey polyclonal, Jackson Immunoresearch) and CF680 anti-rabbit (1:1,000 or 1:500, goat F(ab)′ fragment, Sigma-Aldrich). The samples were mounted in a custom sample holder and imaged in blinking buffer (50 mM Tris HCl, pH 8, 10 mM NaCl, 10% (wt/vol) D-glucose, 500 µg/ml glucose oxidase, 40 µg/ml catalase, and 35 mM mercaptoethylamine).

SMLM imaging

SMLM data were acquired at room temperature on a custom-built microscope (Deschamps et al., 2016) equipped with a high-NA oil-immersion objective (160×/1.43 NA; Leica). The sample was excited by a Luxx 638-nm laser coming from a laser combiner (LightHub; Omicron-Laserage Laserprodukte) and an additional booster laser (iBEAM-SMART-640-S, Toptica Photonics). The two lasers were combined by a polarizing beam splitter, focused on a speckle reducer (LSR-3005-17S-VIS; Optotune), and coupled into a multimode fiber (M105L02S-A; Thorlabs). The output of the multimode fiber was first magnified by an achromatic lens and then focused onto the sample. The beam was cleaned from fiber-generated fluorescence with a laser cleanup filter (390/482/563/640 HC Quad; AHF). Emitted fluorescence was separated by a 4× dichroic mirror and split ratiometrically by a 665-nm longpass dichroic mirror (Chroma, ET665lp). After the 665LP dichroic mirror, the transmitted and reflected photons were filtered with a 685/70 (Chroma ET685/70m) and a 676/37 (Semrock, FF01-676/37-25) filter, respectively. The fluorescence emission was recorded by an electron-multiplying charge-coupled device camera (Photometrics, Evolve512D). For 3D SMLM, an astigmatic lens (f = 1,000 mm, Thorlabs) was placed in the emission beam path. The focus was stabilized by totally internally reflecting an infrared laser on the coverslip and detecting it on a quadrant photodiode. The quadrant photodiode was in a closed feedback loop with the piezo objective positioner (Physik Instrumente). A field-programmable gate array (Mojo; Embedded Micro) was used to control the lasers, switch filters, and stabilize the

focus. The field programmable gate array is controlled by a custom-written plugin for μManager (Edelstein et al., 2010). Typically, we acquired 100,000–150,000 frames with an exposure time of 15 ms and laser power densities of ~6 kW/cm².

Processing of SMLM data

All postprocessing of raw data was performed using the custom-written software SMAP (Superresolution Microscopy Analysis Platform, https://github.com/jries/SMAP). Before the super-resolution experiment, bead stacks were acquired to generate a model of the astigmatic point spread function (Li et al., 2018). To localize the molecules, peaks are first detected by a difference of Gaussian algorithm. These peaks are then fitted globally across both channels with the previously generated point spread function. The z positions of the emitters are linked between the two channels, whereas the x and y coordinates are taken only from the transmitted channel. Subsequently, localizations are filtered by their localization precision and their z position to reject dim and out-of-focus emitters. Emitters that were localized within 35 nm in consecutive frames were grouped into one displayed localization with a maximal dark time of 1 frame. Sample drift was corrected by a custom algorithm based on redundant cross-correlation. For this, the localizations were binned in time, and the superresolved image for each bin was reconstructed. Then, the pairwise cross-correlation of each image against each other image was calculated and fitted by a spline to correct the x and y coordinates. The axial drift was corrected by redundant 1D cross-correlations. The color of the individual fluorophores was assigned according to their relative brightness in the two channels. The superresolved image was reconstructed by plotting Gaussians at the fitted positions with a width proportional to their localization precision.

Data analysis

To map the localization of protein domains within the SC, individual regions of interest corresponding to SCs in frontal view were selected from dual-color SMLM images of late-pachytene nuclei (identified by the presence of bright GFP-COSA-1 foci). To this end, regions of interest containing two clearly separated, parallel, and straight stretches of HIM-3 localizations, corresponding to axes in frontal view, were selected. The total length and number of individual stretches are summarized in Fig. S3 A. Individual stretches were rotated and aligned using a custom script in R (version 3.6.0). To determine the positions of individual protein domains, their localization densities in frontal (x) and cross-sectional (z) views were fitted by unimodal or bimodal Gaussian distributions to obtain peak-to-peak distances (d, for bimodal distributions only) and widths (HWHM). SDs of these parameters were determined by a bootstrapping approach (Köhler et al., 2017).

Statistical analysis

Statistical analysis was performed using Prism 8 (GraphPad). For the analysis of the distance between COSA-1 foci in *mnT12* fusion chromosomes (Fig. 8 D), P values were calculated using a two-tailed Mann–Whitney U test, which is a nonparametric statistic ideal for such datasets. For the analysis of CHK-2 active zone shown in Fig. S5 C, normality test was performed using the D'Agostino–Pearson method, and P values were calculated using an ordinary one-way ANOVA. The number of data points (n) is indicated in the figure legends.

Online supplemental material

Fig. S1 shows the coiled-coil prediction and germline expression of SYP-5 and SYP-6. Fig. S2 shows STED microscopy images demonstrating that the C-termini of SYP-5 and SYP-6 also localize between the chromosome axes. Fig. S3 shows the supporting data and measurements for SMLM analyses. Fig. S4 shows the schematics of null alleles generated for *syp-5* and *syp-6* and validation of the SYP-5 and SYP-5/6 antibodies. Fig. S5 shows the impact of SYP-5/6 deletion on meiotic progression and the analysis of C-terminal truncation mutants of *syp-5/6*. Table S1 shows additional hits from the mass spectrometry analysis of SYP-3–interacting proteins. Table S2 lists the alleles generated in this study. Table S3 lists the crRNAs, repair templates, and genotyping primers for mutant alleles generated in this study. Table S4 lists the worm strains used in this study.

References

Altschul, S.F., T.L. Madden, A.A. Schäffer, J. Zhang, Z. Zhang, W. Miller, and D.J. Lipman. 1997. Gapped BLAST and PSI-BLAST: a new generation of protein database search programs. *Nucleic Acids Res.* 25:3389–3402. https://doi.org/10.1093/nar/25.17.3389

Anderson, L.K., S.M. Royer, S.L. Page, K.S. McKim, A. Lai, M.A. Lilly, and R.S. Hawley. 2005. Juxtaposition of C (2) M and the transverse filament

protein C (3) G within the central region of Drosophila synaptonemal complex. *Proc. Natl. Acad. Sci. USA.* 102:4482–4487. https://doi.org/10.1073/pnas.0500172102

Cahoon, C.K., J.M. Helm, and D.E. Libuda. 2019. Synaptonemal complex central region proteins promote localization of pro-crossover factors to recombination events during Caenorhabditis elegans meiosis. *Genetics.* 213:395–409.

Cahoon, C.K., Z. Yu, Y. Wang, F. Guo, J.R. Unruh, B.D. Slaughter, and R.S. Hawley. 2017. Superresolution expansion microscopy reveals the three-dimensional organization of the Drosophila synaptonemal complex. *Proc. Natl. Acad. Sci. USA.* 114:E6857–E6866. https://doi.org/10.1073/pnas.1705623114

Colaiacovo, M.P., A.J. MacQueen, E. Martinez-Perez, K. McDonald, A. Adamo, A. La Volpe, and A.M. Villeneuve. 2003. Synaptonemal Complex Assembly in C. elegans Is Dispensable for Loading Strand-Exchange Proteins but Critical for Proper Completion of Recombination. *Dev. Cell.* 5: 463–474. https://doi.org/10.1016/S1534-5807(03)00232-6

Colaiacovo, M., G. Stanfield, K. Reddy, V. Reinke, S. Kim, and A. Villeneuve. 2002. A targeted RNAi screen for genes involved in chromosome morphogenesis and nuclear organization in the Caenorhabditis elegans germline. *Genetics.* 162:113.

Couteau, F., and M. Zetka. 2005. HTP-1 coordinates synaptonemal complex assembly with homolog alignment during meiosis in C. elegans. *Genes Dev.* 19:2744–2756. https://doi.org/10.1101/gad.1348205

Couteau, F., K. Nabeshima, A. Villeneuve, and M. Zetka. 2004. A Component of C. elegans Meiotic Chromosome Axes at the Interface of Homolog Alignment, Synapsis, Nuclear Reorganization, and Recombination. *Curr. Biol.* 14:585–592. https://doi.org/10.1016/j.cub.2004.03.033

de Vries, F.A.T., E. de Boer, M. van den Bosch, W.M. Baarends, M. Ooms, L. Yuan, J.-G. Liu, A.A. van Zeeland, C. Heyting, and A. Pastink. 2005. Mouse Sycp1 functions in synaptonemal complex assembly, meiotic recombination, and XY body formation. *Genes Dev.* 19:1376–1389. https://doi.org/10.1101/gad.329705

Deschamps, J., A. Rowald, and J. Ries. 2016. Efficient homogeneous illumination and optical sectioning for quantitative single-molecule localization microscopy. *Opt. Express.* 24:28080–28090. https://doi.org/10.1364/OE.24.028080

Dong, H., and G.S. Roeder. 2000. Organization of the Yeast Zip1 Protein within the Central Region of the Synaptonemal Complex. *J. Cell Biol.* 148: 417–426. https://doi.org/10.1083/jcb.148.3.417

Dunce, J.M., O.M. Dunne, M. Ratcliff, C. Millan, S. Madgwick, I. Usón, and O.R. Davies. 2018. Structural basis of meiotic chromosome synapsis through SYCP1 self-assembly. *Nat. Struct. Mol. Biol.* 25:557–569. https://doi.org/10.1038/s41594-018-0078-9

Edelstein, A., N. Amodaj, K. Hoover, R. Vale, and N. Stuurman. 2010. Computer control of microscopes using µManager. *Curr. Protoc. Mol. Biol.* 92: 14.20.11–14.20.17.

Fawcett, D.W. 1956. The fine structure of chromosomes in the meiotic prophase of vertebrate spermatocytes. *J. Biophys. Biochem. Cytol.* 2:403–406. https://doi.org/10.1083/jcb.2.4.403

Force, A., M. Lynch, F.B. Pickett, A. Amores, Y.-l. Yan, and J. Postlethwait. 1999. Preservation of duplicate genes by complementary, degenerative mutations. *Genetics.* 151:1531–1545.

Goldstein, P., and D. Slaton. 1982. The synaptonemal complexes of Caenorhabditis elegans. *Chromosoma.* 84:585–597. https://doi.org/10.1007/BF00292857

Goodyer, W., S. Kaitna, F. Couteau, J.D. Ward, S.J. Boulton, and M. Zetka. 2008. HTP-3 Links DSB Formation with Homolog Pairing and Crossing Over during C. elegans Meiosis. *Dev. Cell.* 14:263–274. https://doi.org/10.1016/j.devcel.2007.11.016

Guindon, S., J.-F. Dufayard, V. Lefort, M. Anisimova, W. Hordijk, and O. Gascuel. 2010. New algorithms and methods to estimate maximum-likelihood phylogenies: assessing the performance of PhyML 3.0. *Syst. Biol.* 59:307–321. https://doi.org/10.1093/sysbio/syq010

Hammarlund, M., M.W. Davis, H. Nguyen, D. Dayton, and E.M. Jorgensen. 2005. Heterozygous insertions alter crossover distribution but allow crossover interference in C. elegans. *Genetics.* 171:1047–1056. https://doi.org/10.1534/genetics.105.044834

Hassold, T., H. Hall, and P. Hunt. 2007. The origin of human aneuploidy: where we have been, where we are going. *Hum. Mol. Genet.* 16(R2): R203–R208. https://doi.org/10.1093/hmg/ddm243

Hayashi, M., S. Mlynarczyk-Evans, and A.M. Villeneuve. 2010. The synaptonemal complex shapes the crossover landscape through cooperative assembly, crossover promotion and crossover inhibition during Caenorhabditis elegans meiosis. *Genetics.* 186:45–58. https://doi.org/10.1534/genetics.110.115501

Hillers, K.J., and A.M. Villeneuve. 2003. Chromosome-Wide Control of Meiotic Crossing over in C. elegans. *Curr. Biol.* 13:1641–1647. https://doi.org/10.1016/j.cub.2003.08.026

Hodgkin, J., H.R. Horvitz, and S. Brenner. 1979. Nondisjunction mutants of the nematode Caenorhabditis elegans. *Genetics.* 91:67–94.

Jeffress, J.K., S.L. Page, S.M. Royer, E.D. Belden, J.P. Blumenstiel, L.K. Anderson, and R.S. Hawley. 2007. The Formation of the Central Element of the Synaptonemal Complex May Occur by Multiple Mechanisms: The Roles of the N- and C-Terminal Domains of the Drosophila C(3)G Protein in Mediating Synapsis and Recombination. *Genetics.* 177:2445–2456. https://doi.org/10.1534/genetics.107.078717

Kaitna, S., P. Pasierbek, M. Jantsch, J. Loidl, and M. Glotzer. 2002. The Aurora B Kinase AIR-2 Regulates Kinetochores during Mitosis and Is Required for Separation of Homologous Chromosomes during Meiosis. *Curr. Biol.* 12:798–812. https://doi.org/10.1016/S0960-9822(02)00820-5

Kim, S.K., J. Lund, M. Kiraly, K. Duke, M. Jiang, J.M. Stuart, A. Eizinger, B.N. Wylie, and G.S. Davidson. 2001. A gene expression map for Caenorhabditis elegans. *Science.* 293:2087–2092. https://doi.org/10.1126/science.1061603

Kim, Y., N. Kostow, and A.F. Dernburg. 2015. The Chromosome Axis Mediates Feedback Control of CHK-2 to Ensure Crossover Formation in C. elegans. *Dev. Cell.* 35:247–261. https://doi.org/10.1016/j.devcel.2015.09.021

Kim, Y., S.C. Rosenberg, C.L. Kugel, N. Kostow, O. Rog, V. Davydov, T.Y. Su, A.F. Dernburg, and K.D. Corbett. 2014. The Chromosome Axis Controls Meiotic Events through a Hierarchical Assembly of HORMA Domain Proteins. *Dev. Cell.* 31:487–502. https://doi.org/10.1016/j.devcel.2014.09.013

Köhler, S., M. Wojcik, K. Xu, and A.F. Dernburg. 2017. Superresolution microscopy reveals the three-dimensional organization of meiotic chromosome axes in intact Caenorhabditis elegans tissue. *Proc. Natl. Acad. Sci. USA.* 114:E4734–E4743.

Kumar, S., G. Stecher, M. Suleski, and S.B. Hedges. 2017. TimeTree: a resource for timelines, timetrees, and divergence times. *Mol. Biol. Evol.* 34: 1812–1819. https://doi.org/10.1093/molbev/msx116

Larkin, M.A., G. Blackshields, N. Brown, R. Chenna, P.A. McGettigan, H. McWilliam, F. Valentin, I.M. Wallace, A. Wilm, and R. Lopez. 2007. Clustal W and Clustal X version 2.0. *Bioinformatics.* 23:2947–2948.

Li, Y., M. Mund, P. Hoess, J. Deschamps, U. Matti, B. Nijmeijer, V.J. Sabinina, J. Ellenberg, I. Schoen, and J. Ries. 2018. Real-time 3D single-molecule localization using experimental point spread functions. *Nat. Methods.* 15:367–369. https://doi.org/10.1038/nmeth.4661

Libuda, D.E., S. Uzawa, B.J. Meyer, and A.M. Villeneuve. 2013. Meiotic chromosome structures constrain and respond to designation of crossover sites. *Nature.* 502:703–706. https://doi.org/10.1038/nature12577

Liu, J.-G., L. Yuan, E. Brundell, B. Björkroth, B. Daneholt, and C. Höög. 1996. Localization of the N-terminus of SCP1 to the central element of the synaptonemal complex and evidence for direct interactions between the N-termini of SCP1 molecules organized head-to-head. *Exp. Cell Res.* 226:11–19. https://doi.org/10.1006/excr.1996.0197

Lynch, M., and J.S. Conery. 2000. The evolutionary fate and consequences of duplicate genes. *Science.* 290:1151–1155. https://doi.org/10.1126/science.290.5494.1151

Lynch, M., and A. Force. 2000. The probability of duplicate gene preservation by subfunctionalization. *Genetics.* 154:459–473.

Machovina, T.S., R. Mainpal, A. Daryabeigi, O. McGovern, D. Paouneskou, S. Labella, M. Zetka, V. Jantsch, and J.L. Yanowitz. 2016. A surveillance system ensures crossover formation in C. elegans. *Curr. Biol.* 26: 2873–2884. https://doi.org/10.1016/j.cub.2016.09.007

MacQueen, A.J., and A.M. Villeneuve. 2001. Nuclear reorganization and homologous chromosome pairing during meiotic prophase require C. elegans chk-2. *Genes Dev.* 15:1674–1687. https://doi.org/10.1101/gad.902601

MacQueen, A.J., M.P. Colaiacovo, K. McDonald, and A.M. Villeneuve. 2002. Synapsis-dependent and -independent mechanisms stabilize homolog pairing during meiotic prophase in C. elegans. *Genes Dev.* 16:2428–2442. https://doi.org/10.1101/gad.1011602

MacQueen, A.J., C.M. Phillips, N. Bhalla, P. Weiser, A.M. Villeneuve, and A.F. Dernburg. 2005. Chromosome sites play dual roles to establish homologous synapsis during meiosis in C. elegans. *Cell.* 123:1037–1050. https://doi.org/10.1016/j.cell.2005.09.034

Martinez-Perez, E., and M.P. Colaiácovo. 2009. Distribution of meiotic recombination events: talking to your neighbors. *Curr. Opin. Genet. Dev.* 19:105–112. https://doi.org/10.1016/j.gde.2009.02.005

Martinez-Perez, E., and A.M. Villeneuve. 2005. HTP-1-dependent constraints coordinate homolog pairing and synapsis and promote chiasma

formation during C. elegans meiosis. *Genes Dev.* 19:2727–2743. https://doi.org/10.1101/gad.1338505

Martinez-Perez, E., M. Schvarzstein, C. Barroso, J. Lightfoot, A.F. Dernburg, and A.M. Villeneuve. 2008. Crossovers trigger a remodeling of meiotic chromosome axis composition that is linked to two-step loss of sister chromatid cohesion. *Genes Dev.* 22:2886–2901. https://doi.org/10.1101/gad.1694108

McDonnell, A.V., T. Jiang, A.E. Keating, and B. Berger. 2006. Paircoil2: improved prediction of coiled coils from sequence. *Bioinformatics.* 22:356–358. https://doi.org/10.1093/bioinformatics/bti797

Moses, M.J. 1956. Chromosomal structures in crayfish spermatocytes. *J. Biophys. Biochem. Cytol.* 2:215–218. https://doi.org/10.1083/jcb.2.2.215

Muller, H.J. 1916. The mechanism of crossing-over. *Am. Nat.* 50:193–221. https://doi.org/10.1086/279534

Nabeshima, K., A. Villeneuve, and K. Hillers. 2004. Chromosome-wide regulation of meiotic crossover formation in Caenorhabditis elegans requires properly assembled chromosome axes. *Genetics.* 168:1275–1292. https://doi.org/10.1534/genetics.104.030700

Nieuwenhuizen, R.P., K.A. Lidke, M. Bates, D.L. Puig, D. Grünwald, S. Stallinga, and B. Rieger. 2013. Measuring image resolution in optical nanoscopy. *Nat. Methods.* 10:557–562. https://doi.org/10.1038/nmeth.2448

Owen, A.B., J. Stuart, K. Mach, A.M. Villeneuve, and S. Kim. 2003. A gene recommender algorithm to identify coexpressed genes in C. elegans. *Genome Res.* 13:1828–1837.

Page, S.L., and R.S. Hawley. 2001. c(3)G encodes a Drosophila synaptonemal complex protein. *Genes Dev.* 15:3130–3143. https://doi.org/10.1101/gad.935001

Page, S.L., and R.S. Hawley. 2004. The genetics and molecular biology of the synaptonemal complex. *Annu. Rev. Cell Dev. Biol.* 20:525–558. https://doi.org/10.1146/annurev.cellbio.19.111301.155141

Papp, B., C. Pal, and L.D. Hurst. 2003. Dosage sensitivity and the evolution of gene families in yeast. *Nature.* 424:194–197. https://doi.org/10.1038/nature01771

Pattabiraman, D., B. Roelens, A. Woglar, and A.M. Villeneuve. 2017. Meiotic recombination modulates the structure and dynamics of the synaptonemal complex during C. elegans meiosis. *PLoS Genet.* 13:e1006670. https://doi.org/10.1371/journal.pgen.1006670

Phillips, C.M., C. Wong, N. Bhalla, P.M. Carlton, P. Weiser, P.M. Meneely, and A.F. Dernburg. 2005. HIM-8 Binds to the X Chromosome Pairing Center and Mediates Chromosome-Specific Meiotic Synapsis. *Cell.* 123:1051–1063. https://doi.org/10.1016/j.cell.2005.09.035

Rog, O., and A.F. Dernburg. 2015. Direct Visualization Reveals Kinetics of Meiotic Chromosome Synapsis. *Cell Reports.* 10:1639–1645. https://doi.org/10.1016/j.celrep.2015.02.032

Rog, O., S. Köhler, and A.F. Dernburg. 2017. The synaptonemal complex has liquid crystalline properties and spatially regulates meiotic recombination factors. *eLife.* 6:e21455. https://doi.org/10.7554/eLife.21455

Rogers, E., J.D. Bishop, J.A. Waddle, J.M. Schumacher, and R. Lin. 2002. The aurora kinase AIR-2 functions in the release of chromosome cohesion in Caenorhabditis elegans meiosis. *J. Cell Biol.* 157:219–229. https://doi.org/10.1083/jcb.200110045

Rosu, S., K.A. Zawadzki, E.L. Stamper, D.E. Libuda, A.L. Reese, A.F. Dernburg, and A.M. Villeneuve. 2013. The C. elegans DSB-2 Protein Reveals a Regulatory Network that Controls Competence for Meiotic DSB Formation and Promotes Crossover Assurance. *PLoS Genet.* 9:e1003674. https://doi.org/10.1371/journal.pgen.1003674

Roth, T.F. 1966. Changes in the synaptinemal complex during meiotic prophase in mosquito oocytes. *Protoplasma.* 61:346–386. https://doi.org/10.1007/BF01248989

Schermelleh, L., A. Ferrand, T. Huser, C. Eggeling, M. Sauer, O. Biehlmaier, and G.P. Drummen. 2019. Super-resolution microscopy demystified. *Nat. Cell Biol.* 21:72–84. https://doi.org/10.1038/s41556-018-0251-8

Schild-Prufert, K., T.T. Saito, S. Smolikov, Y. Gu, M. Hincapie, D.E. Hill, M. Vidal, K. McDonald, and M.P. Colaiácovo. 2011. Organization of the Synaptonemal Complex During Meiosis in Caenorhabditis elegans. *Genetics.* 189:411–421. https://doi.org/10.1534/genetics.111.132431

Schücker, K., T. Holm, C. Franke, M. Sauer, and R. Benavente. 2015. Elucidation of synaptonemal complex organization by super-resolution imaging with isotropic resolution. *Proc. Natl. Acad. Sci. USA.* 112:2029–2033. https://doi.org/10.1073/pnas.1414814112

Shin, Y., and C.P. Brangwynne. 2017. Liquid phase condensation in cell physiology and disease. Science. 357:eaaf4382.

Smolikov, S., A. Eizinger, K. Schild-Prufert, A. Hurlburt, K. McDonald, J. Engebrecht, A.M. Villeneuve, and M.P. Colaiacovo. 2007. SYP-3 Restricts Synaptonemal Complex Assembly to Bridge Paired Chromosome Axes During Meiosis in Caenorhabditis elegans. *Genetics.* 176:2015–2025. https://doi.org/10.1534/genetics.107.072413

Smolikov, S., K. Schild-Prufert, and M.P. Colaiacovo. 2009. A Yeast Two-Hybrid Screen for SYP-3 Interactors Identifies SYP-4, a Component Required for Synaptonemal Complex Assembly and Chiasma Formation in *Caenorhabditis elegans* Meiosis. *PLoS Genet.* 5:e1000669. https://doi.org/10.1371/journal.pgen.1000669

Srayko, M., D.W. Buster, O.A. Bazirgan, F.J. McNally, and P.E. Mains. 2000. MEI-1/MEI-2 katanin-like microtubule severing activity is required for Caenorhabditis elegans meiosis. *Genes Dev.* 14:1072–1084.

Stamper, E.L., S.E. Rodenbusch, S. Rosu, J. Ahringer, A.M. Villeneuve, and A.F. Dernburg. 2013. Identification of DSB-1, a Protein Required for Initiation of Meiotic Recombination in Caenorhabditis elegans, Illuminates a Crossover Assurance Checkpoint. *PLoS Genet.* 9:e1003679. https://doi.org/10.1371/journal.pgen.1003679

Sym, M., and G.S. Roeder. 1994. Crossover interference is abolished in the absence of a synaptonemal complex protein. *Cell.* 79:283–292. https://doi.org/10.1016/0092-8674(94)90197-X

Sym, M., J. Engebrecht, and G.S. Roeder. 1993. ZIP1 is a synaptonemal complex protein required for meiotic chromosome synapsis. *Cell.* 72:365–378. https://doi.org/10.1016/0092-8674(93)90114-6

Szostak, J.W., T.L. Orr-Weaver, R.J. Rothstein, and F.W. Stahl. 1983. The double-strand-break repair model for recombination. *Cell.* 33:25–35. https://doi.org/10.1016/0092-8674(83)90331-8

Tung, K.-S., and G.S. Roeder. 1998. Meiotic chromosome morphology and behavior in zip1 mutants of Saccharomyces cerevisiae. *Genetics.* 149:817–832.

Woglar, A., and A.M. Villeneuve. 2018. Dynamic Architecture of DNA Repair Complexes and the Synaptonemal Complex at Sites of Meiotic Recombination. *Cell.* 173:1678–1691.e16. https://doi.org/10.1016/j.cell.2018.03.066

Yokoo, R., K.A. Zawadzki, K. Nabeshima, M. Drake, S. Arur, and A.M. Villeneuve. 2012. COSA-1 Reveals Robust Homeostasis and Separable Licensing and Reinforcement Steps Governing Meiotic Crossovers. *Cell.* 149:75–87. https://doi.org/10.1016/j.cell.2012.01.052

Zetka, M.C., I. Kawasaki, S. Strome, and F. Muller. 1999. Synapsis and chiasma formation in Caenorhabditis elegans require HIM-3, a meiotic chromosome core component that functions in chromosome segregation. *Genes Dev.* 13:2258–2270. https://doi.org/10.1101/gad.13.17.2258

Zickler, D., and N. Kleckner. 1999. Meiotic chromosomes: integrating structure and function. *Annu. Rev. Genet.* 33:603–754. https://doi.org/10.1146/annurev.genet.33.1.603
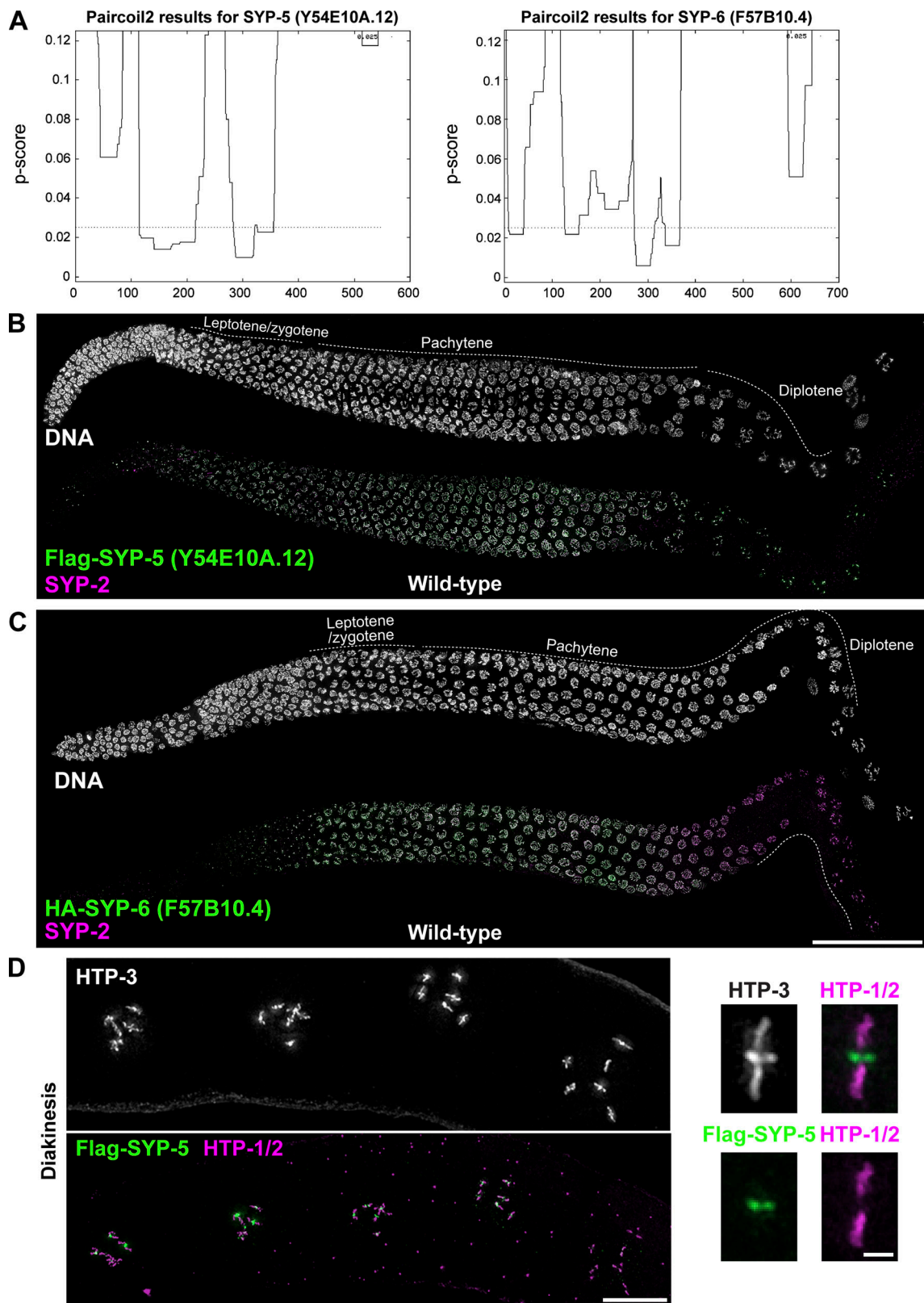
Supplemental material

Figure S1.   **SYP-5 and SYP-6 are localized along the SC in the *C. elegans* germline**. **(A)** Coiled-coil prediction of SYP-5 and SYP-6. P-scores were generated using Paircoil2 (McDonnell et al., 2006). Residues of p-score <0.025 are predicted to be in a coiled-coil. **(B and C)** A whole gonad was dissected from a worm strain expressing Flag-SYP-5 (B) or HA-SYP-6 (C) and stained for DNA (white), SYP-2 (magenta), and Flag-SYP-5 or HA-SYP-6 (green). Composite immuno-fluorescence images are shown. Scale bar, 50 μm. **(D)** Left: Composite immunofluorescence images showing diakinesis nuclei stained for HTP-3 (white), Flag-SYP-5 (green), and HTP-1/2 (magenta). Scale bar, 10 μm. Right: A zoomed-in image of a bivalent showing HTP-3 (white), Flag-SYP-5 (green), and HTP-1/2 (magenta). Scale bar, 2 μm.
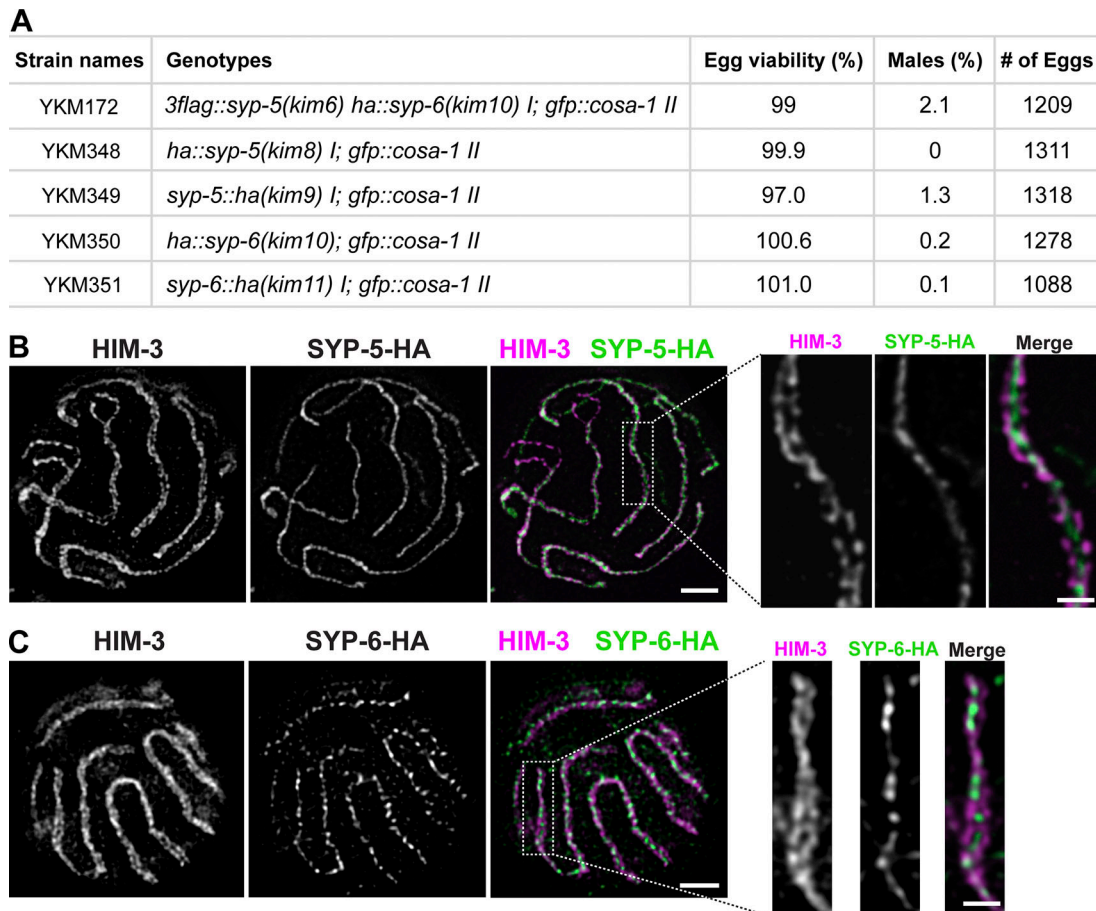
A

Strain names	Genotypes	Egg viability (%)	Males (%)	# of Eggs
YKM172	*3flag::syp-5(kim6) ha::syp-6(kim10) I; gfp::cosa-1 II*	99	2.1	1209
YKM348	*ha::syp-5(kim8) I; gfp::cosa-1 II*	99.9	0	1311
YKM349	*syp-5::ha(kim9) I; gfp::cosa-1 II*	97.0	1.3	1318
YKM350	*ha::syp-6(kim10); gfp::cosa-1 II*	100.6	0.2	1278
YKM351	*syp-6::ha(kim11) I; gfp::cosa-1 II*	101.0	0.1	1088

Figure S2. **STED microscopy of C-terminally tagged SYP-5 and SYP-6. (A)** List of strains used in superresolution microscopy and egg counts. Note that egg viability of >100% is a consequence of failing to count some embryos. **(B and C)** STED microscopy images of pachytene nuclei showing HIM-3 and the HA epitope at the C-termini of SYP-5 (B) or SYP-6 (C). Scale bar, 1 μm. Insets show zoomed-in view of SYP-5 or SYP-6 staining between the two chromosome axes (HIM-3) from the boxed regions. Scale bar, 300 nm.
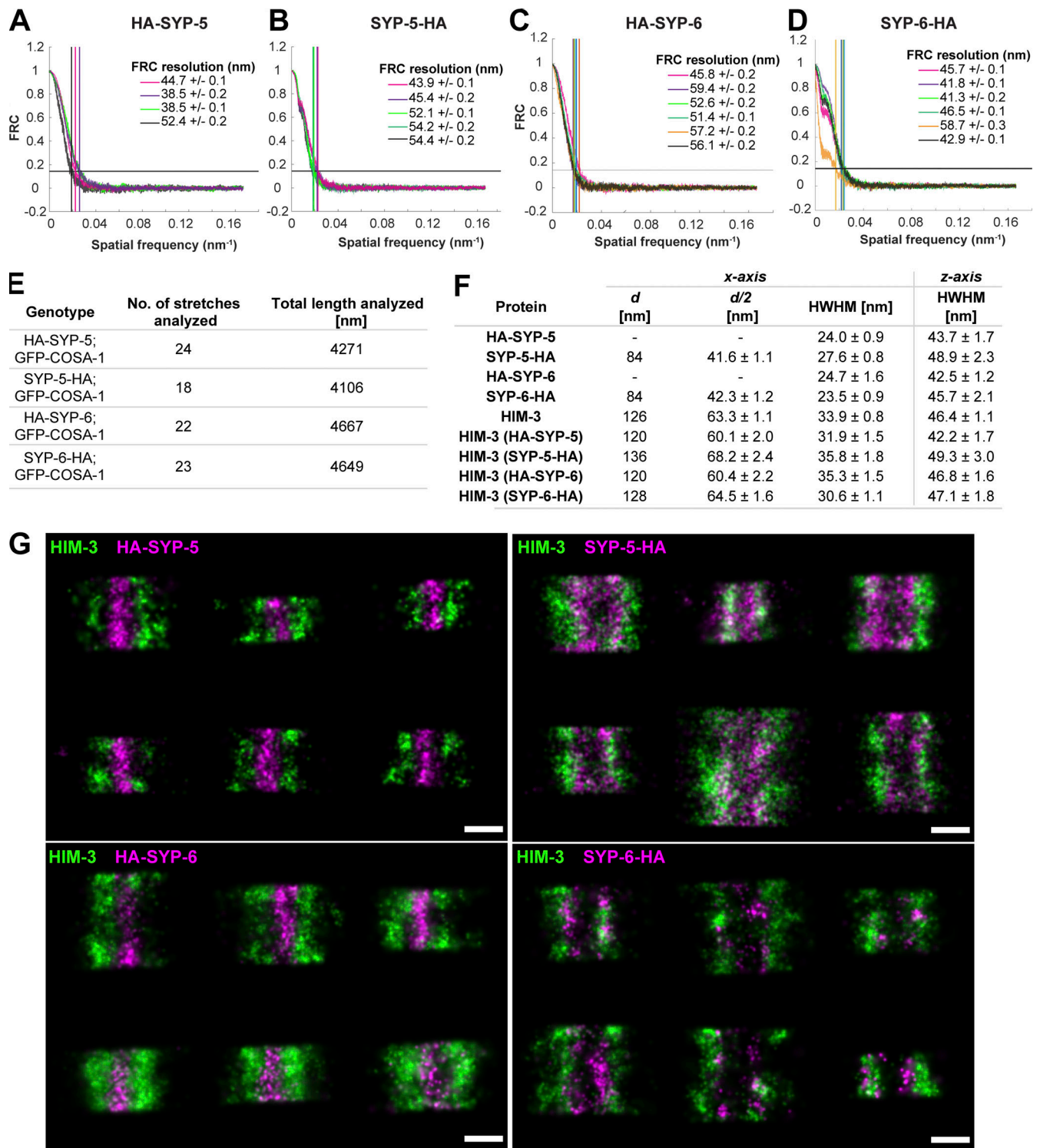
Figure S3. SMLM. (A–D) Plots show the Fourier ring correlation (FRC) curves and the resolution of the SMLM images of N- and C-termini of SYP-5/6 as indicated. **(E)** Number and total length of the stretches that were analyzed to map the orientation of SYP-5 and SYP-6. **(F)** Distribution parameters of the localizations in frontal view (x-axis) and cross-sectional view (z-axis) with SDs obtained by a bootstrapping approach. d, distance between two localization peaks; d/2, distance from the center of the SC; –, unimodal distribution. The width of the distribution is given by the HWHM of the fitted Gaussian distributions. **(G)** Examples of individual stretches taken from SMLM images: HIM-3 (green) and SYP-5/6 (magenta). The stretches were then rotated and aligned to map the positions of N- and C-termini of SYP-5 and SYP-6 (see Materials and methods). Scale bar, 100 nm.
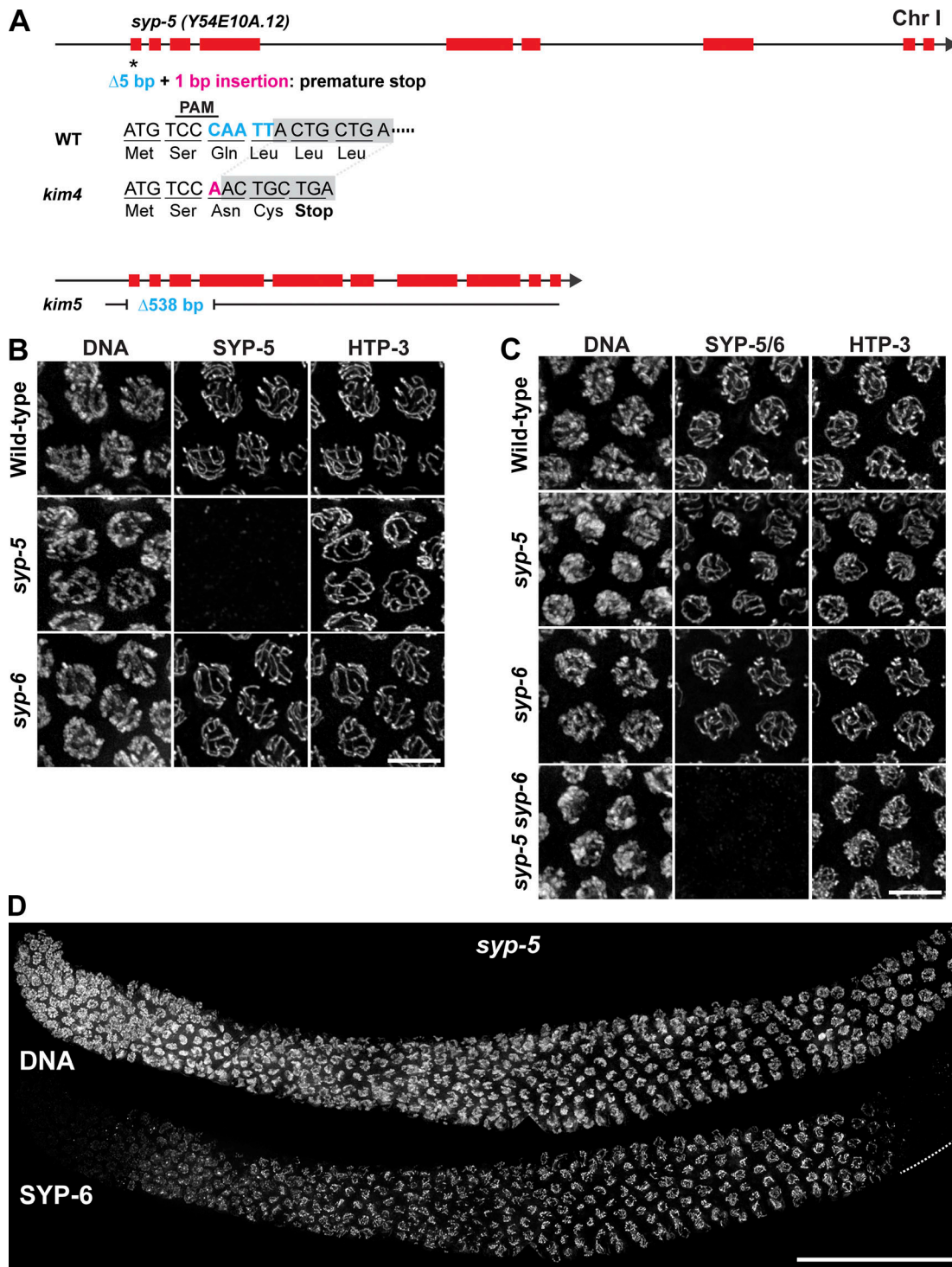
Figure S4. **Generation of null alleles for *syp-5* and *syp-6* and antibody characterization. (A)** Schematic showing the mutagenesis strategy for generating null alleles of *syp-5* and *syp-6*. **(B and C)** Immunofluorescence images of pachytene nuclei from the indicated genotypes stained for DNA, HTP-3, and SYP-5 (B) or SYP-5/6 (C). Scale bars, 5 μm. **(D)** Composite immunofluorescence image of a dissected gonad from a *syp-6* animal stained with DAPI and anti-SYP-5/6 antibody. Scale bar, 50 μm.

A

Genotypes	Egg viability (%)	Males (%)	Number of eggs
N2	100	0.1	1197
syp-5	34	15	1182
syp-6	100	0.2	1254
syp-5 syp-6	3	45	1899

B

C **E** **F**

D

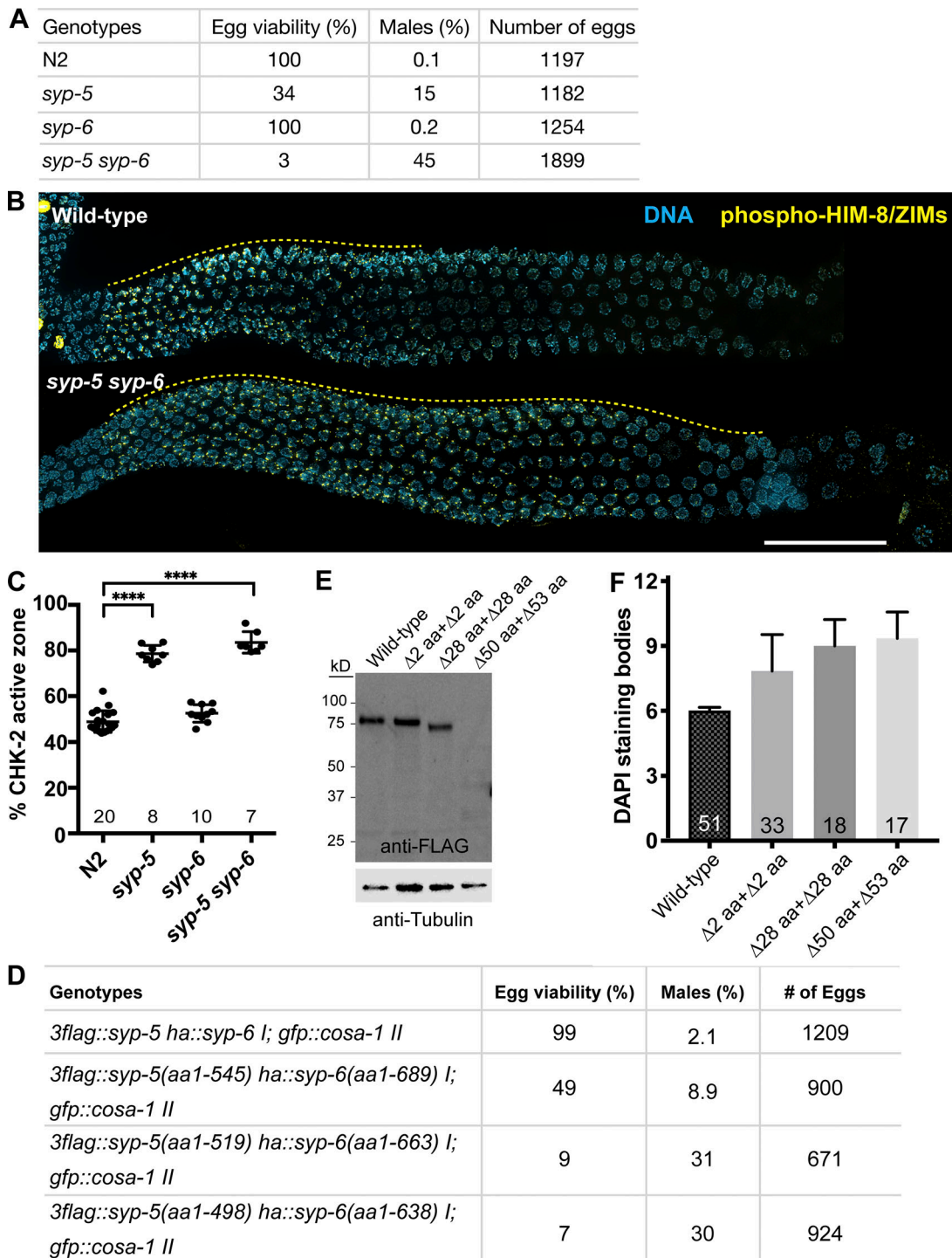| Genotypes	Egg viability (%)	Males (%)	# of Eggs
3flag::syp-5 ha::syp-6 I; gfp::cosa-1 II	99	2.1	1209
3flag::syp-5(aa1-545) ha::syp-6(aa1-689) I; gfp::cosa-1 II	49	8.9	900
3flag::syp-5(aa1-519) ha::syp-6(aa1-663) I; gfp::cosa-1 II	9	31	671
3flag::syp-5(aa1-498) ha::syp-6(aa1-638) I; gfp::cosa-1 II	7	30	924

Figure S5. **Analysis of null and C-terminal truncation mutants of SYP-5 and SYP-6. (A)** Table showing the percentage viable and male self-progeny from *C. elegans* hermaphrodites of indicated genotypes. **(B)** Immunofluorescence of *C. elegans* gonads dissected from wild-type and *syp-5 syp-6* animals stained for DNA (blue) and phosphorylated HIM-8/ZIMs (yellow). Regions of the gonad positive for phospho-HIM-8/ZIMs staining are marked by yellow dotted lines. Scale bar, 50 μm. **(C)** Quantification of CHK-2 active zone in the indicated strains. Numbers of gonads scored are indicated below. Bars indicate mean and SD. Whereas the CHK-2 active zone is significantly increased in *syp-5* and *syp-5 syp-6* double mutants compared with wild-type (****, P < 0.0001), *syp-6* mutants did not show significant difference from wild-type (P = 0.1074) by ordinary one-way ANOVA. **(D)** Table showing the percentage viable and male self-progeny from *C. elegans* hermaphrodites of indicated genotypes. **(E)** Western blot of whole-worm lysates for Flag-tagged SYP-5 truncations. Tubulin was used as a loading control. **(F)** Graph showing the average number of DAPI-staining bodies in diakinesis oocytes from the C-terminal truncation mutants. Numbers of oocytes scored are indicated below. Error bars indicate SD.

Hurlock et al.
Identification of new SC components in *C. elegans*

Journal of Cell Biology S6
https://doi.org/10.1083/jcb.201910043

Provided online are four supplemental tables. Table S1 shows mass spectrometry analysis of SYP-3–interacting proteins. Table S2 lists alleles generated in this study. Table S3 lists crRNAs, repair templates and genotyping primers for mutant alleles generated in this study. Table S4 lists strains used in this study.